The [simple carbon project] model v1.0

Cameron O'Neill[1], Andrew McC. Hogg[1], Michael Ellwood[1], Stephen Eggins[1], and Bradley Opdyke[1]

[1]Research School of Earth Sciences, Australian National University

Correspondence to: Cameron O'Neill (cameron.oneill@anu.edu.au)

Abstract. We construct a carbon cycle box model to process observed or inferred geochemical evidence from modern and paleo settings. The [simple carbon project] model v1.0 ("SCP-M") combines a modern understanding of the ocean circulation regime with the earth's carbon cycle. SCP-M estimates the concentrations of a range of elements within the carbon cycle for use in paleo reconstructions or future projections, by simulating ocean circulation, biological, chemical and atmospheric and terrestrial carbon cycle processes. In this paper we demonstrate the model's application primarily with analysis of the Last Glacial Maximum (LGM) to Holocene carbon cycle transition, and also with the modern carbon cycle under the influence of anthropogenic emissions. The model is shown to be capable of reproducing both paleo and modern observations, and aligns with CMIP5 model projections. We conduct an atmospheric and ocean multi-proxy data-model parameter optimisation for the LGM and late Holocene periods, using the growing pool of published paleo atmosphere and ocean data for CO_2, $\delta^{13}C$, $\Delta^{14}C$ and carbonate ion proxy. The results provide strong evidence for an ocean-wide physical mechanism to deliver the LGM to Holocene carbon cycle transition. Alongside ancillary changes in ocean temperature, volume, salinity, sea ice cover and atmospheric radiocarbon production rate, changes in global overturning circulation, and, to a lesser extent Atlantic meridional overturning circulation, can drive the observed LGM and late Holocene signals in atmospheric CO_2, $\delta^{13}C$, $\Delta^{14}C$, and the oceanic distribution of $\delta^{13}C$, $\Delta^{14}C$ and carbonate ion proxy. Further work is needed on analysis and processing of ocean proxy data to improve confidence in these modelling results, but this preliminary use of SCP-M suggests that a solution to the LGM-Holocene dilemma is close at hand.

1 Introduction

The LGM-Holocene dilemma, and interglacial variations in the carbon cycle in general, remains one of the great outstanding problems in oceanography (e.g. Sigman and Boyle, 2000; Hain et al., 2010; Ferrari et al., 2014). At issue is the precise cause of 80-100 ppm variations in atmospheric CO_2 across glacial and interglacial periods. These CO_2 oscillations are accompanied by striking changes in ocean and atmospheric carbon isotopes, oceanic carbonate ion distributions and other paleo chemical indicators. Of particular interest is the transition from the LGM, ∼18-24 kyr ago (Yokoyama et al., 2000; Hesse et al., 2011), to the Holocene (11.7 kyr- present), due to the growing abundance of proxy data covering that period. 'The dilemma', is that the causes of abrupt atmospheric CO_2 rise at the termination of the LGM, and continuing up to the Holocene period, remain definitively unresolved. The ocean is likely the main driver of atmospheric CO_2 on the relevant timescale, due to its relative size as a carbon reservoir (Sigman et al., 2010). Active theories within the ocean realm include changes in ocean biology,

ocean circulation and mixing, sea ice cover or whole ocean chemistry (Sigman et al., 2010). Each of these are supported by site-specific tracer observations, regional data aggregation and review, or modelling. Within the spectrum, a simple explanation of an oceanic carbon mechanism remains elusive. Many of the hypotheses are presented as independent, or even competing in causality for the interglacial CO_2 variation (Ferrari et al., 2014). Modelling exercises have failed to properly resolve the

5 problem due to poor data constraints (particularly for the ocean), overly-complicated, inflexible models that cannot account for key drivers of the proxy data signals in the earth's carbon system (e.g. carbon isotopes and carbonate ion), or adequately incorporate a sufficient quantum of data across multiple proxies. Many of these studies have focussed on atmospheric CO_2 data, with only qualitative reference to the ocean data, thereby allowing solutions by many different oceanic mechanisms to remain in play. We propose to advance the debate by using a carbon cycle box model specifically designed to leverage available

10 ocean and atmosphere geochemical data, and we see this approach as particularly valuable in light of the fast growing paleo-data pool.

Box models have proven invaluable in understanding the global carbon cycle. A box model divides regions of the ocean into boxes or grids, based on some property of the composite water masses, such as temperature, density or chemical composition. The model equations describe the evolution of tracers in the model's boxes, due to the various fluxes between each box (Fig.

15 1). Box models range in complexity from simple (Toggweiler, 1999) to more complex (Hain et al., 2010) ocean models to full carbon cycle models (Zeebe, 2012). Box models, despite being simpler than their General Circulation Model (GCM) counterparts, have been useful in illustrating key concepts in oceanography that were pioneering in their time. For example, Sarmiento and Toggweiler (1984), Siegenthaler and Wenk (1984) and Knox and McElroy (1984) used simple four-box ocean-atmosphere models to show that the LGM CO_2 drawdown could have resulted from increased biological productivity and/or

20 reduced ocean overturning circulation. More recently, Hain et al. (2010) used a box model to show that a range of ocean physical and biological mechanisms were required to cause lower atmospheric CO_2 levels in the LGM, and Zhao et al. (2017) used a similar model to explore ocean ventilation ages in the LGM-deglacial and Holocene periods.

Our motivation in constructing a new box model of the full carbon cycle, the [simple carbon project] model v1.0 ("SCP-M"), is to contribute a simple, easy to use, open access model implemented with freely available software, that is consistent

25 with physical and biogeochemical oceanography, that caters for important features of the ocean and extra-ocean carbon cycle, and has explicit avenues for data integration, optimisation and inversion. The model-data experiment described in this paper provides a direct linkage between paleo-data and discrete values for ocean parameters in the LGM and late Holocene periods, thus potentially resolving the LGM-Holocene dilemma. Combined with the growing dataset of paleo observations, and with advances in computing power, data-aligned models such as SCP-M have the potential to improve our understanding of past

30 changes in climate across many other timeframes. Furthermore, SCP-M is computationally cheap and quick to run. For example a 10,000 year simulation takes approximately thirty seconds to process on a regular laptop.

In this paper we describe the SCP-M model and illustrate its application alongside LGM and late Holocene period ocean and atmosphere data, with several insights for the transition between the two periods, plus modelling of the modern and future carbon cycle under the influence of anthropogenic emissions. Emphasis is placed on the model description and configuration.

2 SCP-M description

SCP-M is focussed on the ocean carbon cycle and is configured to estimate the time evolution of elemental concentrations of oceanic dissolved inorganic carbon (DIC) and its constituents, δ^{13}C, Δ^{14}C, plus alkalinity, phosphorus, oxygen and atmospheric CO_2, δ^{13}C, and Δ^{14}C. It contains a simple, yet realistic representation of large scale ocean physical processes, with an overlay of ocean chemistry and biology. SCP-M simulates sources and sinks of carbon across ocean and atmosphere, marine sediments, terrestrial biosphere, volcanic emissions, sedimentary weathering and riverine fluxes, and anthropogenic emissions. This approach is chosen because the concentration of carbon in the ocean and atmosphere (and its isotopes in particular) are sensitive to all sources and sinks, and omitting them makes it difficult to compare model results with the carbon data that indelibly features their imprint. For example, regrowth in the terrestrial biosphere imparts a clear signature on the atmosphere and ocean δ^{13}C data profile after the LGM (Francois et al., 1999). In addition, the atmospheric radiocarbon source, marine sediments, volcanic emissions, continental weathering, and now anthropogenic emissions, exert important influences on carbon cycle observations.

SCP-M was designed to compare model results with data, and to solve for optimal parameter combinations. As such, more emphasis is placed on a realistic implementation of the model parameters, ease of data integrations and on representation of the important features of the carbon cycle than on precise *a priori* estimation of the starting input values. Realistic implementation of physical processes within a sound biogeochemical platform enables their transmission into paleo-chemical tracer signals, for which proxy data exists. Many of the key ocean physical and biological processes are prescribed in the model, allowing them to be free parameters in model-data experiments. SCP-M itself is implemented with a matrix framework which enables more boxes to be added, ocean basins to be separated, elements to be added, exploration of a range of hypotheses, all with minimal programming effort. The model is presently zonally averaged to elucidate information about the large scale processes operating across all of the ocean basins.

2.1 Model topology

The box model is mostly conceptual in nature and is designed to test high-level concepts. Therefore, excessive detail and complication is to be avoided. However, key processes that are critical to the validity of any thesis being tested, must be represented as well as possible. The ocean is a key part of the global carbon cycle and pre-eminent in hypotheses of the LGM-Holocene dilemma (Sigman et al., 2010) and we focus the model's detail there.

Talley (2013) provided an observationally-based description of ocean circulation in terms of its constituent water masses, circulation and mixing fluxes, and including estimates of the present day magnitudes of those fluxes. The Talley (2013) model builds on the models of Broecker (1991), Gordon (1991), Schmitz (1996), Lumpkin and Speer (2007), Kuhlbrodt et al. (2007), Talley (2008), and Marshall and Speer (2012). Key features of the Talley (2013) model include:

- Atlantic thermocline water moves north ultimately reaching the North Atlantic, driven by advection and surface buoyancy changes. High salinity North Atlantic Deep Water (NADW) forms in the north by cooling, densification and convection,
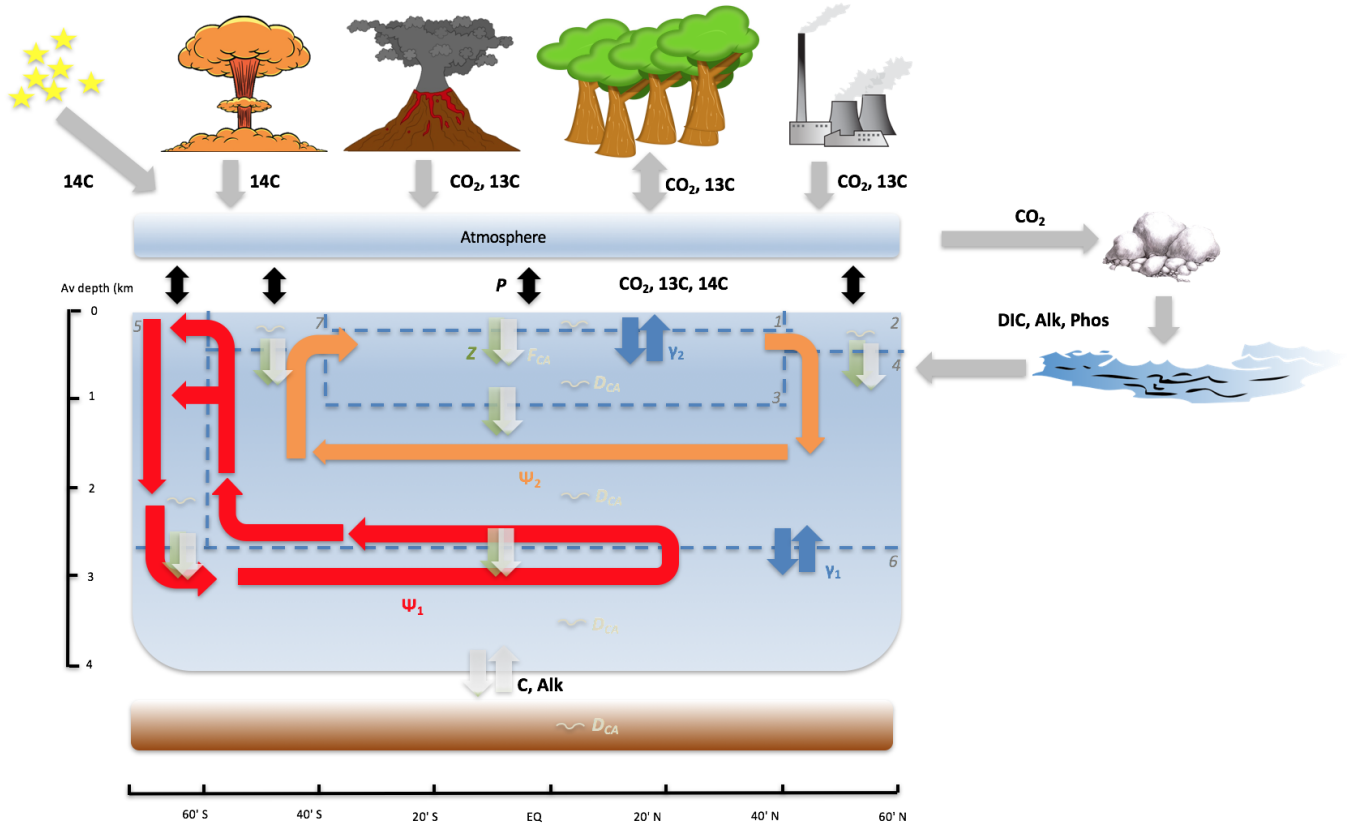
Figure 1. SCP-M: configured as a seven box ocean model-plus atmosphere with marine sediments, continents and the terrestrial biosphere. Exchange of elemental concentrations, e.g. $C_i, (i = 1, 7)$ occur due to fluxes between boxes. Ψ_1 is global overturning circulation, Ψ_2 is Atlantic meridional overturning circulation (AMOC), γ_1 is deep-abyssal mixing, γ_2 is low-latitude thermohaline mixing, Z is the biological pump, F_{CA} is the rain ratio, D_{CA} is carbonate dissolution and P is the air-sea gas exchange. Box 1 = low latitude/tropical surface ocean, box 2 = northern surface ocean, box 3 = intermediate ocean, box 4 = deep ocean, box 5 = Southern Ocean, box 6 = abyssal ocean, box 7 = sub polar southern surface ocean.

and then travels south to rise up into the Southern Ocean via wind-driven upwelling and Ekman flows, forming Lower Circumpolar Deep Water (LCDW). This water comprises the upper (orange arrows) overturning circulation in Fig. 1.

– A fraction of the upwelled LCDW sinks to become Antarctic Bottom Water (AABW) under the influence of cooling and brine rejection, south of the Antarctic Circumpolar Current (ACC). AABW moves northward along the ocean floor via adiabatic advection (Talley, 2013) in all basins. It upwells into IDW/PDW in the Pacific and Indian Oceans and also into NADW in the Atlantic via upwelling with diapycnal diffusion (Talley, 2013).

- Pacific Deep Water/Indian Deep Water (PDW/IDW) upwells at low latitudes and returns to the Southern Ocean above the NADW, forming the core of the Upper Circumpolar Deep Water (UCDW), which is identified by Talley (2013) as low oxygen content (old) water. A part of the upwelled PDW/IDW joins NADW/AABW formation, with the bulk of it moving northward at the sea surface to provide the key northward flux out of the Southern Ocean. These waters are freshened and warmed, and join Antarctic Intermediate Water (AAIW) and Subantarctic Mode Water (SAMW) at the base of the subtropical thermocline (advection with surface buoyancy fluxes). The combined LCDW/AABW/PDW/IDW overturning circulation is represented by the red arrows in Fig. 1.

- Joined thermocline waters, AAIW/Subantarctic Mode Water (SAMW) and upwelled thermocline waters from the Pacific and Indian Oceans, form the upper ocean transport moving towards the North Atlantic.

A key contribution of the Talley (2013) study is that global overturning circulation is the pre-eminent process in distributing water throughout the global oceans. Talley (2013) provided a zonally-averaged, 2-D 'collapsed' interpretation of a 3-D ocean layout, based on the observation that similar, large scale processes (i.e. global overturning circulation) operate in all three major ocean basins, and this interpretation can directly inform a box model topology. The Talley (2013) 2-D global ocean view, used in SCP-M, captures the features described above in a zonally-averaged ocean box model format. Talley (2013) also provided observation-based estimates of the ocean transport fluxes, which are scaled according to their ocean basin domain. For example, the global overturning circulation and AABW-formation process is common to all basins, and thus accounts for the largest flux, of 29 Sv. The AMOC/NADW sinking cell is confined to the Atlantic Basin and represents a smaller flux, 19 Sv, of water.

The SCP-M dimensions are designed to be consistent with measured estimates of the surface area and average depth of the ocean, and total ocean and atmosphere volumes. SCP-M contains seven ocean boxes as shown in Fig. 1. The rationale for dividing the ocean into boxes is that there are regions of the ocean that are relatively well mixed, or at least similar in terms of their prevailing element flux behaviour. For the depth of the surface boxes, this rationale conveniently translates to the maximum wintertime mixed layer depth (MLD). We choose a depth of 100m for Box 1, the low latitude surface box, which is a reasonable approximation to the 20-150m seasonally-varying MLD for the mid and low latitudes estimated by de Boyer Montegut et al. (2004), and consistent with the depth of a similar box in the Toggweiler (1999) model. This box represents the photic zone over much of the ocean, from 40°S to 40°N. Craig (1957) estimated the depth of this layer as 75m ±25m, a value used by Keeling and Bolin (1968) in their simple ocean box model. We choose 250m depth for the NADW box (box 2) and the sub polar surface box (box 7) as per Toggweiler (1999). These boxes are deeper than the low latitude surface box (de Boyer Montegut et al., 2004), in order to capture the regions of deep water upwelling (sub polar Southern Ocean) and convective downwelling (North Atlantic). The MLD in these regions can vary between 70 and >500m depth depending on seasonal variations (de Boyer Montegut et al., 2004). An intermediate depth box (3) resides below the low latitude surface box and extends from 100m depth to 1000m depth. This box captures northward flowing AAIW and SAMW from upwelled NADW/PDW/IDW (e.g. Talley, 2013). Box 4 is the deep ocean box, extending from 1,000m depth to 2,500m depth and incorporates the upwelling abyssal waters in all basins, and downwelled NADW. This water is channeled back to the surface

in the sub polar surface box and the Southern Ocean box, as per the wind-driven upwelling of Morrison and Hogg (2013) and Talley (2013). The Southern Ocean box (5) extends from 80°S to 60°S and from the ocean surface to 2,500m depth. This box encompasses the Southern Ocean, the ACC and deep water formation from southward flowing upwelled NADW/PDW/IDW (Talley, 2013). The abyssal box (6) extends the full range of the ocean, from 2,500m to 4,000m depth (our assumed average

5   depth of the ocean). This box is the pathway for northward flowing AABW and incorporates mixing with overlying deep water and advection/upwelling (Talley, 2013).

2.2   The model parameters, processes and equations

2.2.1   Basic features

Figure 2 shows the suite of files used to execute SCP-M. We have chosen a modular approach to reduce complexity of each

10   of the model files. The SCP-M routine includes data processing for the model's boxes on the model's geographic coordinates, model calibration to the data, model simulations, model-data optimisation and charting/tabular output. SCP-M is implemented in Python 3.6, with the code and download/user instructions available at (https://doi.org/10.5281/zenodo.1310161).
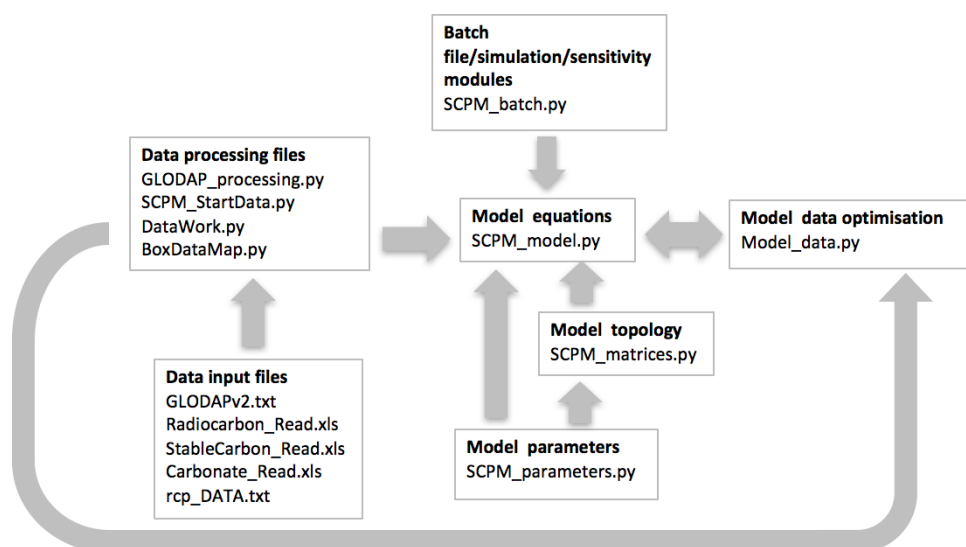
Figure 2. SCP-M Python and ancillary files with their linkages. SCP-M is currently implement in Python 3.6, although has been run on other versions of Python. Folder/file structure structure separates model and data files. All files and user manual are available from (https://doi.org/10.5281/zenodo.1310161).

In short, SCP-M calculates the evolution of an element's or species' concentration in each model box, as a function of time and flux parameters (e.g. inputs and outputs to each box), or processes, such as uptake or regeneration. The model includes

ocean circulation and mixing fluxes, air-sea gas exchange, chemical and biological transformations, and sources and sinks of carbon.

2.2.2 The ocean circulation and mixing

There are four ocean physical parameters in SCP-M. Ψ_1 and Ψ_2 are advection terms that represent the physical transport of
5 water from one box to another, containing the element or species concentration of its box of origin. Ψ_1 represents the global ocean overturning circulation (e.g. Sarmiento and Toggweiler, 1984; Marshall and Speer, 2012; Talley, 2013) that infiltrates all basins (Talley, 2013) and is shown by the red arrows in Fig. 1. The Ψ_1 parameter allows a variable allocation between transport from the deep ocean box (box 4) into the sub-polar surface box (box 7) and directly into the polar box (box 5), via α. The α parameter is set by default to 0.50, such that 50 per cent of the upwelling flow Ψ_1 is directed into the sub polar surface box,
10 and 50 per cent is directed into the southern polar box. Ψ_2 represents Atlantic Meridional Overturning Circulation (AMOC). This is the region of North Atlantic Deep Water (NADW) formation of Dickson and Brown (1994) and Talley (2013), shown as orange arrows in Fig. 1. γ_1 and γ_2 are bidirectional mixing terms that exchange element or species concentrations between boxes without any net advection of water (blue arrows in Fig. 1). γ_1 is bidirectional mixing between the deep and abyssal boxes of the form described by Lund et al. (2011) and De Boer and Hogg (2014). γ_2 is a low latitude, intermediate-shallow
15 box "thermocline" mixing parameter, which governs the constant bidirectional exchange between these two boxes (Liu et al., 2016).

The influence of each of the ocean parameters is prescribed in box model space by matrix equations, with one matrix for each parameter. Each row and column position in the matrix corresponds to a box location. The atmosphere box is treated separately from the ocean boxes, and it does not enter the ocean parameter matrices. The volumetric circulation or mixing
20 parameters, in Sv (10^6 m^3 s^{-1}) are multiplied by the oceanic element concentration (mol m^{-3}) to produce a molar flux of elements between ocean boxes. For example the change in concentration of carbon (as DIC) in the deep box (box 4) from ocean physical parameters is estimated by:

$$\left[\frac{dC_4}{dt}\right]_{phys} = \frac{\Psi_1(C_6 - C_4)}{V_4} + \frac{\Psi_2(C_2 - C_4)}{V_4} + \frac{\gamma_1(C_6 - C_4)}{V_4} \tag{1}$$

where C_i is the concentration of carbon in each box in mol m^{-3} and V_i is the volume of each box in m^3. For the low latitude
25 surface box:

$$\left[\frac{dC_1}{dt}\right]_{phys} = \frac{\gamma_2(C_3 - C_1)}{V_1} \tag{2}$$

These operations can be vectorised using sparse matrices, as follows:

$$\left[\frac{d\mathbf{C}}{dt}\right]_{phys} = \frac{(\Psi_1\mathsf{T}_1 + \Psi_2\mathsf{T}_2 + \gamma_1\mathsf{E}_1 + \gamma_2\mathsf{E}_2) \cdot \mathbf{C}}{\mathbf{V}} \tag{3}$$

where:

30 $\mathbf{C} = C_i, \, for \, i = 1,7$ \hfill (4)

$$\mathbf{V} = V_i, \; for \; i = 1,7 \tag{5}$$

and T_1, T_2, E_1 and E_2 are sparse matrices defined as:

$$\mathsf{T1} = \begin{pmatrix} 0 & 0 & 0 & 0 & 0 & 0 & 0 \\ 0 & 0 & 0 & 0 & 0 & 0 & 0 \\ 0 & 0 & 0 & 0 & 0 & 0 & 0 \\ 0 & 0 & 0 & -1 & 0 & 1 & 0 \\ 0 & 0 & 0 & (1-\alpha) & -1 & 0 & \alpha \\ 0 & 0 & 0 & 0 & 1 & -1 & 0 \\ 0 & 0 & 0 & \alpha & 0 & 0 & -\alpha \end{pmatrix} \tag{6}$$

$$\mathsf{T2} = \begin{pmatrix} 0 & 0 & 0 & 0 & 0 & 0 & 0 \\ 0 & -1 & 1 & 0 & 0 & 0 & 0 \\ 0 & 0 & -1 & 0 & 0 & 0 & 1 \\ 0 & 1 & 0 & -1 & 0 & 0 & 0 \\ 0 & 0 & 0 & 0 & 0 & 0 & 0 \\ 0 & 0 & 0 & 0 & 0 & 0 & 0 \\ 0 & 0 & 0 & 1 & 0 & 0 & -1 \end{pmatrix} \tag{7}$$

$$\mathsf{E1} = \begin{pmatrix} 0 & 0 & 0 & 0 & 0 & 0 & 0 \\ 0 & 0 & 0 & 0 & 0 & 0 & 0 \\ 0 & 0 & 0 & 0 & 0 & 0 & 0 \\ 0 & 0 & 0 & -1 & 0 & 1 & 0 \\ 0 & 0 & 0 & 0 & 0 & 0 & 0 \\ 0 & 0 & 0 & 1 & 0 & -1 & 0 \\ 0 & 0 & 0 & 0 & 0 & 0 & 0 \end{pmatrix} \tag{8}$$

10 $$\mathsf{E2} = \begin{pmatrix} -1 & 0 & 1 & 0 & 0 & 0 & 0 \\ 0 & 0 & 0 & 0 & 0 & 0 & 0 \\ 1 & 0 & -1 & 0 & 0 & 0 & 0 \\ 0 & 0 & 0 & 0 & 0 & 0 & 0 \\ 0 & 0 & 0 & 0 & 0 & 0 & 0 \\ 0 & 0 & 0 & 0 & 0 & 0 & 0 \\ 0 & 0 & 0 & 0 & 0 & 0 & 0 \end{pmatrix} \tag{9}$$

2.2.3 Biological flux parameter

The biological pump (e.g. Broecker, 1982) is the action of marine biological activity to utilise nutrients in shallow waters, die, sink and then release those nutrients at depth. For example, through photosynthesis carbon is taken up by shallow water-dwelling phytoplankton and then sequestered in deeper waters after sinking, breaking down and re-mineralising their nutrient load back into the water column. Volk and Hoffert (1985) made the distinction between the soft tissue pump (STP), for soft tissued organisms, and the carbonate pump (carbonate-shelled organisms). We also distinguish between the two, as they have different effects on carbon and alkalinity balances and therefore pCO$_2$ and carbonate dissolution. This section deals with the STP, and a following section deals with the carbonate pump. Most STP organic matter is remineralised in the shallow to intermediate ocean depths, leading to a decrease in the export of carbon as depth increases. According to Henson et al. (2011), only $\sim$15-25 per cent of organic material is exported to >100m depth, with most recycled in the shallower waters.

   Martin et al. (1987) modelled the soft-bodied organic flux of carbon observed from sediment traps in the northeast Pacific to create a simple power rule which is easily applicable to modelling purposes. The Martin et al. (1987) equation produces a flux of organic carbon which is a function of depth from a base organic flux at 100m depth (the "Martin reference depth"). The flux at 100m depth was estimated by Martin et al. (1987) to be between 1.2 and 7.1 mol C m^{-2} yr^{-1} from eight station observations in the northeast Pacific. Sarmiento and Gruber (2006) estimated a range of 0.0 - 5.0 mol C m^{-2} yr^{-1}, and some localised higher values, across the global ocean. Equation (10) shows the general form of the Martin et al. (1987) equation:

$$F = F_{100}\left(\frac{z}{100}\right)^b \tag{10}$$

Where F is a flux of carbon in mol C m^{-2} yr^{-1}, F_{100} is an estimate of carbon flux at 100m depth, z is depth in metres and b is a depth scalar. In SCP-M, the Z parameter implements the Martin et al. (1987) equation. Z is an estimate of biological productivity at 100m depth (in mol C m^{-2} yr^{-1}), and coupled with the Martin et al. (1987) depth scalar, controls the amount of organic carbon that sinks from each model surface box to the boxes below. Each sub surface ocean box receives a flux of carbon from the box above it, at its ceiling depth (also the floor of the overlying box), and loses carbon as a function of the depth of the bottom of the box. Remineralisation in each box is accounted for as the difference between the influx and out-flux of organic carbon. The biological flux out of the surface box 1 is shown by:

$$\left[\frac{dC_1}{dt}\right]_{bio} = \frac{Z_1 S_1 \left(\frac{d_{f1}}{d_0}\right)^b}{V_1} \tag{11}$$

where Z_1 is the biological flux of carbon prescribed for the surface Box 1 in mol C m^{-2} yr^{-1}, S_1 is the surface area of the surface Box 1, d_0 is the reference depth of 100m for the Z parameter value (Martin et al., 1987) and d_c and d_f are the ceiling and floor depths of a box, respectively. The parameter b is the depth power function of the Martin et al. (1987) equation, estimated by Berelson (2001) with an ocean mean value of -0.82 ± 0.16 (dimensionless). The scalar parameter tapers biological production and export below depths of 100m. The net biological flux for intermediate depth Box 3 is given by:

$$\left[\frac{dC_3}{dt}\right]_{bio} = \frac{Z_1 S_1 \left[\left(\frac{d_{c3}}{d_0}\right)^b - \left(\frac{d_{f3}}{d_0}\right)^b\right]}{V_3} \tag{12}$$

The process is vectorised using sparse matrices in the following:

$$\left[\frac{d\mathbf{C}}{dt}\right]_{bio} = \frac{\mathbf{ZS} \cdot (\mathbf{B}_{out} + \mathbf{B}_{in})}{\mathbf{V}} \tag{13}$$

where $\mathbf{Z}$ is an array of the Z_i (i=1,7) parameter which varies across the surface boxes and $\mathbf{S}$ is the array of surface box surface areas S_i (i=1,7). As with the ocean parameters, the biological flux of carbon is divided through by the box volume array $\mathbf{V}$ to return concentrations in mol m^{-3}. $\mathbf{B}_{out}$ and $\mathbf{B}_{in}$ are sparse matrices as follows:

$$\mathbf{B}_{out} = \begin{pmatrix} -(\frac{d_{f1}}{d_0})^{-b} & 0 & 0 & 0 & 0 & 0 & 0 \\ 0 & -(\frac{d_{f2}}{d_0})^{-b} & 0 & 0 & 0 & 0 & 0 \\ -(\frac{d_{f3}}{d_0})^{-b} & 0 & 0 & 0 & 0 & 0 & 0 \\ -(\frac{d_{f4}}{d_0})^{-b} & -(\frac{d_{f4}}{d_0})^{-b} & 0 & 0 & 0 & 0 & -(\frac{d_{f4}}{d_0})^{-b} \\ 0 & 0 & 0 & 0 & -(\frac{d_{f5}}{d_0})^{-b} & 0 & 0 \\ 0 & 0 & 0 & 0 & 0 & 0 & 0 \\ 0 & 0 & 0 & 0 & 0 & 0 & -(\frac{d_{f7}}{d_0})^{-b} \end{pmatrix} \tag{14}$$

$$\mathbf{B}_{in} = \begin{pmatrix} 0 & 0 & 0 & 0 & 0 & 0 & 0 \\ 0 & 0 & 0 & 0 & 0 & 0 & 0 \\ (\frac{d_{c3}}{d_0})^{-b} & 0 & 0 & 0 & 0 & 0 & 0 \\ (\frac{d_{c4}}{d_0})^{-b} & (\frac{d_{c4}}{d_0})^{-b} & 0 & 0 & 0 & 0 & (\frac{d_{c4}}{d_0})^{-b} \\ 0 & 0 & 0 & 0 & 0 & 0 & 0 \\ (\frac{d_{c6}}{d_0})^{-b} & (\frac{d_{c6}}{d_0})^{-b} & 0 & 0 & (\frac{d_{c6}}{d_0})^{-b} & 0 & (\frac{d_{c6}}{d_0})^{-b} \\ 0 & 0 & 0 & 0 & 0 & 0 & 0 \end{pmatrix} \tag{15}$$

The absolute strength of the parameter Z is allowed to vary across the surface boxes as a fraction of the base value specified for Z (presently 5.0 mol C yr^{-1}), with higher fractions in the northern and southern oceans, and smaller fractions in the low latitude and polar oceans (e.g. Sarmiento and Gruber, 2006). The biological flux of other elements and species such as phosphorous and alkalinity, are calculated from the biological carbon flux using so-called "Redfield ratios" (e.g. Redfield et al., 1963; Takahashi et al., 1985; Anderson and Sarmiento, 1994).

2.3 pCO$_2$ and carbonate

The estimation of air-sea gas exchange, atmospheric pCO$_2$ and the "carbonate pump", rest on a realistic estimation of pCO$_2$ in the ocean. For example, only a fraction of dissolved inorganic carbon (DIC) in seawater can exchange with the atmosphere, and this fraction is estimated by the oceanic pCO$_2$. DIC itself consists of three major constituents: carbonic acid, bicarbonate and carbonate. Their relative proportions depend on total DIC, alkalinity, pH, temperature and salinity (Zeebe and Wolf-Gladrow, 2001).

pCO$_2$ is roughly estimated by subtracting alkalinity from DIC. However, this is only accurate to $\pm$10 per cent (Sarmiento and Gruber, 2006), which may cause problems for scenario analysis and sensitivity testing within such a large error band. More complex calculations can require numerous iterations and can be computationally expensive (e.g. Toggweiler and Sarmiento, 1985; Zeebe and Wolf-Gladrow, 2001; Follows et al., 2006). We apply the routine of Follows et al. (2006) in SCP-M, which is

5 a direct solution, rather than an iterative approach to solve for pCO$_2$ at each time step of a model run, which was demonstrated by Follows et al. (2006) to be sufficiently accurate for modelling purposes.

Solving for pCO$_2$ enables the calculation of the concentrations of the three species of DIC, which further enables estimation of the dissolution and burial of carbonate in the water column and sediments. The latter is an important part of the oceanic carbon and alkalinity cycles and provides important feedbacks to atmospheric CO$_2$ on thousand year timeframes (e.g. Farrell

10 and Prell, 1989; Anderson et al., 2007; Mekik et al., 2012; Yu et al., 2014b).

2.3.1 The carbonate pump

According to Emerson and Hedges (2003), $\sim$20-30 per cent of CaCO$_3$ formed in the ocean's surface is preserved in ocean floor sediments, with the rest dissolved in the water column. Klaas and Archer (2002) estimated that 80 per cent of the organic matter fluxes in the ocean below 2,000m are driven by organic matter associated with ballast. Therefore, the so-called "carbonate

15 pump" is a relatively efficient transport of carbon and alkalinity in the ocean. However, according to Farrell and Prell (1989) it is also a dynamic process, for example around glacial cycles, with increased dissolution of CaCO$_3$ during glacial periods and attenuation in interglacials, lending it some interest in the LGM-Holocene dilemma and carbon cycle modelling more broadly.

To replicate this flux of carbon and alkalinity, a term is added to the carbon cycle equation to represent the flux of calcium carbonate (shells) out of the surface boxes into the abyssal box and sediments. This is an extension of the surface organic

20 carbon flux Z described in Eq. (13), via the "rain ratio" parameter. The rain ratio is a common term in ocean biogeochemistry (e.g. Archer and Maier-Reimer, 1994) and refers to the ratio between shell-based 'hard' carbon and organic 'soft' carbon fluxes in the biologically-driven rain of carbon from the ocean's surface. Sarmiento et al. (2002) estimated a global average value for the rain ratio of 0.06 $\pm$0.03, with local maxima and minima of 0.10 and 0.02, respectively, providing a narrow range of global values. We apply the rain ratio as a parameter multiplied by the organic flux parameter Z. The combination delivers the

25 physical production and export of calcium carbonate at the Martin reference depth (100m).

Once the production and export flux at the Martin reference depth is established, the distribution of calcium carbonate in the boxes below is a function of dissolution. According to Milliman et al. (1999), the theory that calcium carbonate only dissolves at great depths in carbonate-undersaturated water is "*one of the oldest and most strongly held paradigms in oceanography*" (e.g. Sverdrup et al., 1941). However, in nature, the alkalinity and carbonate ion concentration profiles suggest that 30-60%

30 of carbonate produced is dissolved in shallower water that is saturated (Harrison et al., 1993; Milliman et al., 1999). Theories for this outcome include, the emergence of locally undersaturated waters due to remineralisation of biological carbon (Jansen et al., 2002), or, dissolution by zooplankton grazing (Milliman et al., 1999). Battaglia et al. (2016) found similar skill in model results for replicating observed dissolution profiles, whether a non- or saturation-dependent dissolution constant was used. Battaglia et al. (2016) recommended the use of a basic non-saturation dependent (i.e. constant) dissolution parameter in earth

carbon system models for computing efficiency, with limited loss of accuracy. As such, we include two parts to the dissolution equation, a non-saturation-dependent dissolution constant, to reflect the 'unknown' processes that likely cause the observed dissolution of calcium carbonate in waters that are saturated, and a saturation state-dependent component, using the dissolution function of Morse and Berner (1972). We include the latter to enable dynamic feedback to take place in the carbonate system

5   after model perturbations. The saturation-dependent dissolution is a function of the average carbonate ion composition for each box, relative to its temperature and pressure-dependent saturation concentration (Morse and Berner, 1972; Millero, 1983). We choose the median depth of each box for the calculation in the ocean boxes, and the floor of the abyssal box for the sediment surface dissolution. We assume 100% of calcium carbonate takes the form of calcite. If the surface export flux of CaCO$_3$ is greater than dissolution in the ocean boxes, then the remainder escapes to the sediments. This is a flux out of the ocean

10   of alkalinity and carbon in the ratio of 2:1 assumed for carbonate shells (Sarmiento and Gruber, 2006). DIC and alkalinity can return to the abyssal box from the sediments via undersaturation-driven dissolution in the abyssal water overlying the sediments.

The net flux of carbonate, between ocean boxes and out of the ocean and into the sediments, is shown in vectorised Eq. (16):

$$\left[\frac{d\mathbf{C}}{dt}\right]_{carb} = \frac{(F_{CA}\mathbf{ZS})}{\mathbf{V}} + (\zeta + \epsilon)\mathbf{CaCO_3} \tag{16}$$

where F_{CA} is the rain ratio, ζ is the constant background dissolution rate, ϵ is the saturation state-dependent dissolution function of Morse and Berner (1972) and Millero (1983) and $\mathbf{CaCO_3}$ is the concentration of calcium carbonate in each box. The dissolution equation of Morse and Berner (1972) operates on CaCO$_3$, which is calculated by multiplying Ca by CO$_3^{2-}$, where Ca is estimated from salinity in each box as per Sarmiento and Gruber (2006).

20   **2.3.2   Air-sea gas exchange**

CO$_2$ is transported across the air-sea interface by gaseous exchange. According to Henry's Law, the partial pressure of a gas [P] above a liquid in thermodynamic equilibrium, will be directly proportional to the concentration of the gas in the liquid:

$$[P] = K_H C \tag{17}$$

where K_H is the solubility of a gas in mmol m^{-3} atm^{-1} and C is its concentration in the liquid. Many ocean models specify the

25   air-sea gas exchange of CO$_2$ as a function of the pCO$_2$ differential between ocean and atmosphere, a CO$_2$ solubility coefficient (e.g. Weiss, 1974), and a so-called "piston" or gas transfer velocity, which governs the rate of gas exchange, in m s^{-1} (e.g. Toggweiler, 1999; Zeebe, 2012; Hain et al., 2010; Watson et al., 2015). We adopt the same approach in estimating the exchange of CO$_2$ between a surface box and the atmosphere:

$$\left[\frac{dC_1}{dt}\right]_{gas} = P_1 S_1 K_{0_1}(pCO_{2_{at}} - pCO_{2_1})\rho \tag{18}$$

30   where P_1 is the piston velocity parameter in Box 1 in m s^{-1}. P varies by surface box to allow for scenario analysis, for example variable sea-ice cover in the polar box. K_{0_1} is the solubility of CO$_2$ in mol kg^{-1} atm^{-1} (Weiss, 1974), subsequently converted

into mol m^{-3} by multiplying by sea water density ρ. pCO_{2_1} and $pCO_{2_{at}}$ are the partial pressures of CO$_2$ in the surface ocean box 1 and atmosphere, respectively, in ppm. The equation is vectorised as follows:

$$\left[\frac{d\mathbf{C}}{dt}\right]_{gas} = \mathbf{PSK_0}(pCO_{2_{at}} - \mathbf{pCO_2})\rho \tag{19}$$

where $\mathbf{P} = P_i$ (i=1,7) with zero values for non-surface boxes, and $\mathbf{K}_0 = K_{0_i}$ (i=1,7).

5 2.4 Extra ocean carbon cycle

SCP-M incorporates the terrestrial biosphere, continental weathering and river run-off into the ocean, plus an atmospheric radiocarbon source, volcanic and industrial emissions.

V is a constant, prescribed flux of volcanic emissions of CO$_2$, in SCP-M. Toggweiler (2007) estimated this volcanic flux of CO$_2$ emissions at $4.98\text{x}10^{12}$ mol year^{-1} using a carbon cycle model which balanced volcanic emissions with land-based

10 weathering sinks. The weathering of carbonate and silicate rocks also creates DIC and alkalinity runoff into the rivers, which find its way into the ocean (Amiotte Suchet et al., 2003). Relative alkalinity and DIC concentrations affect ocean pCO$_2$ and carbonate ion levels, which impacts atmospheric CO$_2$ and the dissolution and burial of carbonates (Sarmiento and Gruber, 2006). We apply the approach of Toggweiler (2007) whereby silicate and carbonate weathering fluxes of DIC and alkalinity make their way only into the low latitude surface ocean box (box 1):

15 $$\left[\frac{dC_1}{dt}\right]_{weath} = (W_{SC} + (W_{SV} + W_{CV})AtCO_2) \tag{20}$$

where W_{SC} is a constant silicate weathering term set at $0.75\text{x}10^{-4}$ mol m^{-3} year^{-1}, W_{SV} is a variable rate of silicate weathering per unit of atmosphere CO$_2$ (ppm), set to 0.5 mol m^{-3} atm^{-1} CO$_2$ year^{-1} and W_{CV} is the variable rate of carbonate weathering with respect to atmosphere CO$_2$, set at 2 mol m^{-3} atm^{-1} CO$_2$ year^{-1} (Toggweiler, 2007).

Alkalinity is added to the ocean in the ratio of 2:1 to DIC (Toggweiler (2007). In the case of silicate rocks, weathering is also

20 a weak sink of CO$_2$ (e.g. Toggweiler, 2007; Hogg, 2008). The atmospheric sink of CO$_2$ is calculated by multiplying Eq. (20) by the volume of the low latitude surface ocean box (box 1) and subtracting from atmospheric CO$_2$. Equation (20) is vectorised by multiplying by a vector of boxes with only a non zero value for box 1.

The terrestrial biosphere may act as a sink of CO$_2$ during periods of biosphere growth (e.g. post glacial regrowth) via carbon fertilisation or a source of CO$_2$ (e.g. glacial reduction) via respiration. We employ a two part model of the terrestrial biosphere

25 with a long term (woody forest) and short term (grassland) terrestrial biosphere box as per Raupach et al. (2011) and Harman et al. (2011), and with net primary productivity (NPP) and respiration parameters controlling the balance between uptake and release of carbon. NPP is positively affected by atmospheric CO$_2$, the so-called "carbon fertilisation" effect, as per Raupach et al. (2011). Respiration is assumed proportional to the carbon stock. The biosphere also preferentially partitions the lighter carbon isotope ^{12}C, leading to a relative enrichment in δ^{13}C in the atmosphere during net uptake of CO$_2$. The change in

30 atmospheric CO$_2$ from the terrestrial biosphere in the model is given by:

$$\left[\frac{dAtCO_2}{dt}\right]_{NPP} = -N_{pre}RP[1 + \beta LN(\frac{AtCO_2}{AtCO_{2pre}})] + \frac{C_{stock1}}{k_1} + D_{forest} \tag{21}$$

Where N_{pre} is NPP at a reference level ("pre") of atmospheric CO_2, RP is the parameter to split NPP between the short term terrestrial biosphere carbon stock (fast respiration) and the longer term stock (slow respiration), after Raupach et al. (2011). β is a parameter with a value typically 0.4-0.8 (Harman et al., 2011), C_{stock1} is the short term carbon stock and k_1 is the respiration timeframe for the short term carbon stock (in years). For the long term terrestrial biosphere, we substitute $(1-RP)$

5 in place of RP and C_{stock2} and k_2 for the long term carbon stock and respiration rate, respectively. D_{forest} is a prescribed flux of deforestation emissions, which can be switched on or off in SCP-M. A $\delta^{13}C$ fractionation factor is applied to the terrestrial biosphere fluxes of carbon, effecting an increase in atmospheric $\delta^{13}C$ from biosphere growth, and a decrease from respiration.

2.5 The complete carbon cycle equations

Equation (22) shows the full vectorised model equation for the calculation of the evolution of carbon concentration in the ocean

10 boxes, incorporating Eq. (1-21).

$$\frac{d(\mathbf{C})}{dt} = \left[\frac{d\mathbf{C}}{dt}\right]_{phys} + \left[\frac{d\mathbf{C}}{dt}\right]_{bio} + \left[\frac{d\mathbf{C}}{dt}\right]_{carb} + \left[\frac{d\mathbf{C}}{dt}\right]_{gas} + \left[\frac{d\mathbf{C}}{dt}\right]_{weath} \tag{22}$$

The calculation of atmospheric CO_2 is:

$$\frac{dAtCO_2}{dt} = \left[\frac{dAtCO_2}{dt}\right]_{gas} + \left[\frac{dAtCO_2}{dt}\right]_{NPP} + \left[\frac{dAtCO_2}{dt}\right]_{volcs} + \left[\frac{dAtCO_2}{dt}\right]_{weath} + \left[\frac{dAtCO_2}{dt}\right]_{anth} \tag{23}$$

where the additional term $\left[\frac{dAtCO_2}{dt}\right]_{anth}$ consists of a prescribed flux of $\delta^{13}C$-depleted and 14C-dead CO_2 to the atmosphere

15 from human industrial emissions, which is activated by a model switch in SCP-M. Additional model equations for carbon isotopes are shown in the Appendix.

3 Modelling results

The modern carbon cycle has been extensively modelled as part of efforts to understand the impact of human emissions on climate. There is abundant data on emissions and detailed observations of the modern carbon cycle with globally coordinated

20 ocean surveys and land-based measuring stations. In addition, numerous modelling exercises, using agreed emissions projection scenarios from the Intergovernmental Panel on Climate Change (IPCC), have created a body of modelling inputs and results. This provides an ideal testing ground for SCP-M. We first calibrate the model for the preindustrial period, then simulate historical and projected human emissions under a number of scenarios.

3.1 Preindustrial calibration

25 We choose the late Holocene period (6-0.2 kya) for our calibration because it has relatively good proxy data coverage (e.g. Table 1) and a relatively steady climate in the absence of perturbations such as industrial CO_2 emissions, bomb radiocarbon or glacial terminations. The late Holocene is also close to the preindustrial period (1700's) in order to act as a starting point

Indicator	Reference
Atmosphere CO_2	Marcott et al. (2014), Scripps CO_2 Program
Atmosphere $\delta^{13}C$	Schmitt et al. (2012), Scripps CO_2 Program
Atmosphere $\Delta^{14}C$	Stuiver et al. (1998), Reimer et al. (2009), Turnbull et al. (2016)
Ocean $\delta^{13}C$	Peterson et al. (2014)
Ocean $\Delta^{14}C$	Skinner and Shackleton (2004); Marchitto et al. (2007); Barker et al. (2010); Bryan et al. (2010); Skinner et al. (2010); Burke and Robinson (2012); Davies-Walczak et al. (2014); Skinner et al. (2015); Chen et al. (2015); Hines et al. (2015); Sikes et al. (2016), Ronge et al. (2016), Skinner et al. (2017)
Ocean carbonate ion	Yu et al. (2014b), Yu et al. (2014a)
Modern ocean data (e.g. DIC, alkalinity, phosphorus, $\delta^{13}C$, $\Delta^{14}C$)	GLODAPv2 (Olsen et al., 2016)
Suess and bomb radiocarbon effect corrections	Broecker et al. (1980), Key (2001), Sabine et al. (2004), Eide et al. (2017)

Table 1. Ocean and atmosphere data sources for the SCP-M modern carbon cycle calibration, projections and LGM-Holocene experiment. The late Holocene is chosen as the initial model calibration to the absence of industrial-era CO_2 and bomb radiocarbon. Scripps CO_2 Program data originally sourced from http://scrippsco2.ucsd.edu, data currently being transitioned to http://cdiac.ess-dive.lbl.gov. The Peterson et al. (2014) database incorporates ∼500 core records across the LGM and late Holocene periods.

for modern carbon cycle simulations, as well as paleo. To calibrate the model for the late Holocene we begin with the modern day GLODAPv2 dataset (https://www.nodc.noaa.gov/ocads/oceans/GLODAPv2/) which we average into the model's boxes on depth and latitude coordinates, using one of the SCP-M scripts (Fig. 2). The GLODAPv2 database incorporates data from ∼1 million seawater samples from 700 cruises over the years 1972-2013, including data from the original GLODAP dataset, plus

5   CARINA and PACIFICA datasets (Olsen et al., 2016). We assume an average data year of 1990 for the data accumulated over the period 1972-2013. We make adjustments to the ocean concentrations of DIC, $\delta^{13}C$ and $\Delta^{14}C$ for the effects of industrial emissions (the "Suess" effect) and bomb radiocarbon in the atmosphere using published estimates (Broecker et al., 1980; Key, 2001; Sabine et al., 2004; Eide et al., 2017). For example, Eide et al. (2017) establishes a mathematical relationship between Suess $\delta^{13}C$ and CFC-12 in the ocean, which we applied using GLODAP CFC-12 data to correct the ocean $\delta^{13}C$ data. We force

10   the model with late Holocene average data for atmosphere CO_2, $\delta^{13}C$ and $\Delta^{14}C$ (data sources in Table 1). The model's starting parameters are set from literature values (Table 4, Appendix), including the point estimates for ocean circulation and mixing fluxes from Talley (2013).

Using the Suess- and bomb- adjusted GLODAP ocean dataset, and late Holocene atmosphere data, as the starting point,

15   combined with the literature-determined parameter values, the model is allowed to run freely for 15 kyr in spin-up. This is ample

time for model equilibrium and to allow slower processes such as carbonate compensation to take effect. The resulting model equilibrium ocean and atmosphere element concentrations from the spin-up are automatically stored and are subsequently carried forward as the starting data for subsequent late Holocene simulations. Figure 3 shows the results of the model spin up (red stars), compared with late Holocene atmosphere data and their standard error (blue dots and error bars) across the

5   time period. We also show the model results compared with late Holocene ocean data from various sources (Table 1) which is averaged into the box model regions for comparison.

The late Holocene calibration convincingly satisfies the atmospheric data values for CO_2, $\delta^{13}C$ and $\Delta^{14}C$. Model results are also in good agreement with the Late Holocene atmosphere and ocean $\Delta^{14}C$, falling within error or very close for all boxes covered by data. The surface boxes (1, 2) are relatively enriched in $\Delta^{14}C$ relative to deeper boxes, reflecting their proximity

10   to the atmospheric source of 14C, although the spread of values across the ocean boxes is narrow. The surface boxes (1, 2 and 7) intuitively display more enriched $\delta^{13}C$ than the intermediate (3), deep (4) and abyssal (6) boxes, mainly due to the effects of the biological pump. For most of the model's boxes, the results fall within the standard error of the late Holocene data. The Southern Ocean box (5), is an exception due to its extensive vertical coverage of 2,500m incorporating the surface boundary with the atmosphere and the deep ocean, coupled with the sparse $\delta^{13}C$ core data for the polar Southern Ocean (one data point,

15   no error bars). SCP-M also exaggerates the depletion in $\delta^{13}C$ in the deep box (4), relative to the data observation.

There is limited data coverage for carbonate ion proxy (CO_3^{2-}), although the model replicates the available data well. CO_3^{2-} concentrations are roughly approximated by alkalinity less DIC (Zeebe and Wolf-Gladrow, 2001; Yu et al., 2014b). CO_3^{2-} is relatively abundant in the surface boxes (e.g. boxes 1 and 2) due to the higher amount of alkalinity relative to carbon, itself resulting from the export activity of the biological pump which prioritises carbon over alkalinity. CO_3^{2-} is less abundant in the

20   deep ocean (boxes 4 and 6), because there is more carbon relative to alkalinity due to remineralisation of the biological pump, which corresponds to lower CO_3^{2-} values, a pattern that SCP-M simulates.

3.2   Sensitivity tests

We varied parameter values around their modern day settings in 10 kyr model runs, and plotted the output against atmospheric CO_2, $\Delta^{14}C$ and $\delta^{13}C$ (Fig. 4). Atmospheric CO_2 is very sensitive to Ψ_1 and Ψ_2 but displays limited response to γ_1 and γ_2 over

25   the ranges analysed (Fig. 4(a-d)). Atmospheric $\Delta^{14}C$ and $\delta^{13}C$ are negatively related to Ψ_1 and Ψ_2. The slower ocean turnover leads to a reduced rate of upwelling and surface de-gassing of $\Delta^{14}C$- and $\delta^{13}C$-depleted waters, causing higher values in the atmosphere. The effect of the mixing parameters on the atmosphere variables is muted because they have limited impact on the upwelling regime for carbon, with any upward flux of carbon offset by a downward flux (mixing).

Z, the soft tissue pump parameter, displays an inverse relationship with CO_2 (Fig. 4(e)) except for small values of Z, when

30   the flux of shell-based organisms out of the surface boxes via the carbonate pump, and the attendant flux of alkalinity and carbon in the ratio of 2:1, is substantially reduced. The continued flux of alkalinity into the ocean, from continental weathering, coupled with the weaker carbonate pump, leads to a build-up in alkalinity in the ocean and a decrease in pCO2. This is most pronounced in the low latitude box, which has a value for Z which is only a small fraction of the base Z value, which is varied in the sensitivity experiment. Eventually, the lower atmospheric CO_2 leads to decreased weathering and river influx to
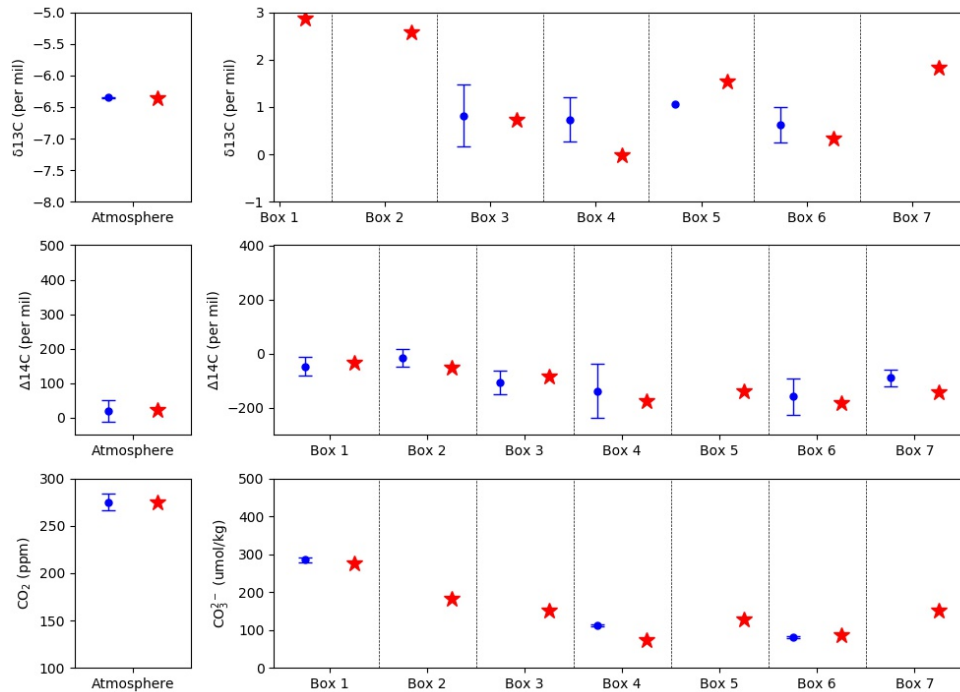
Figure 3. SCP-M late Holocene-calibrated model results using model input parameters from the literature (Table 4). Left panels show model results for atmospheric $\delta^{13}C$, $\Delta^{14}C$ and CO_2 (red stars) plotted against late Holocene average data values (blue dots) with standard error bars. The right panel shows the model results for oceanic $\delta^{13}C$, $\Delta^{14}C$ and carbonate ion proxy (red stars) plotted against late Holocene average ocean data where available (blue dots). Data sources are shown in Table 1.

the ocean, and the carbonate system restores equilibrium. However this takes place over longer timeframes than the sensitivity experiment. If the rain ratio were allowed to increase, in the presence of higher carbonate ion values in the ocean, the effect would be partially mitigated. In the current version of SCP-M, the rain ratio is prescribed. Increasing the base value of the biological pump above 4 mol C m^{-2} yr^{-1} increases the removal of carbon from the surface ocean and also the atmospheric

5   CO_2 flux into the ocean. $\delta^{13}C$ is particularly sensitive to Z, moving it well away from modern (and therefore Holocene and LGM) values from a minor perturbation. Reducing the rain ratio (Fig. 4(f)) drastically lowers CO_2 and increases $\Delta^{14}C$, but also heavily depletes the atmosphere in $\delta^{13}C$.

Increasing surface ocean box temperatures (Fig. 4(g-i)) increases atmospheric CO_2, an intuitive outcome given that warmer water absorbs less CO_2 (Weiss, 1974), and SCP-M employs a temperature- and salinity- dependent CO_2-solubility function.

10   Air-sea fractionation of $\delta^{13}C$ also deceases with higher temperatures, leading to higher atmospheric $\delta^{13}C$. According to Mook et al. (1974), air-to-sea fractionation of $\delta^{13}C$ (making the atmosphere more depleted in $\delta^{13}C$) increases at a rate of approximately 0.1‰ °C^{-1} of cooling. SCP-M employs temperature-dependent air-sea gas $\delta^{13}C$ fractionation factors (Mook et al., 1974). $\Delta^{14}C$ is invariant to box temperature as the fractionation parameters employed in the model are non temperature depen-
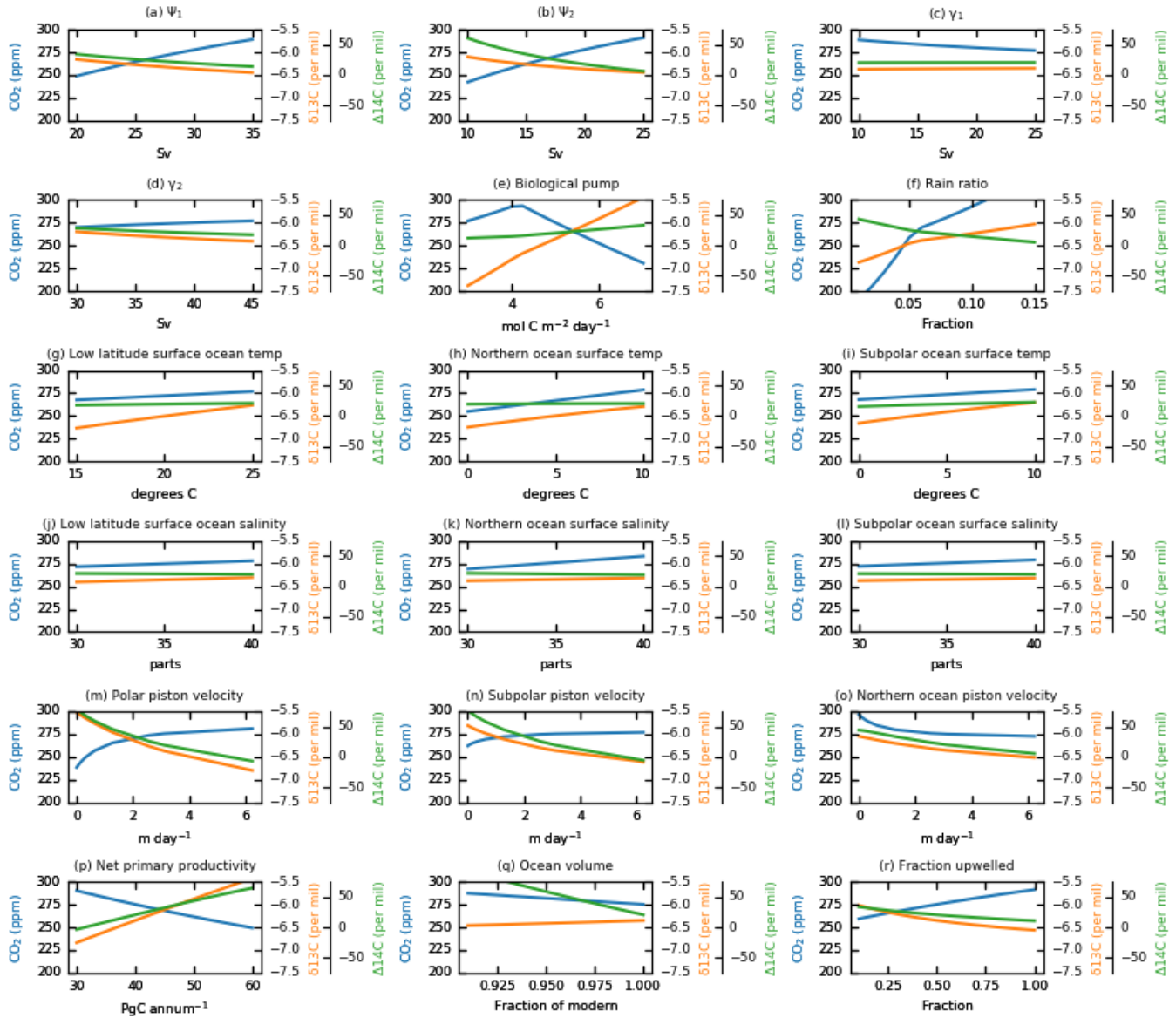
Figure 4. Univariate parameter sensitivity tests around modern day estimated values, plotted for atmospheric CO_2, $\Delta^{14}C$ and $\delta^{13}C$. We varied parameter input values as plotted on the x-axes and show model output for atmospheric CO_2, $\Delta^{14}C$ and $\delta^{13}C$. Atmospheric CO_2 show the greatest sensitivity to parameters associated with ocean circulation, biology and the terrestrial biosphere. Other parameters exert less influence on atmospheric CO_2 but are important for atmospheric carbon isotope values.

dent. CO_2 displays a weak positive relationship with surface ocean box salinity (Fig. 4(j-l)), due to the decreasing solubility of CO_2 in ocean water with increasing salinity (Weiss, 1974).

The piston velocity (P) drives atmospheric carbon isotope values, more than CO_2 itself. As P slows down (Fig. 4(m-o)), atmospheric CO_2 falls modestly, because the polar and sub polar boxes, which are the primary regions of outgassing due to the upwelling of deep-sourced carbon-rich water into those boxes, exchange CO_2 with the atmosphere at a slower rate. The reduced outgassing of $\delta^{13}C$-depleted carbon to the atmosphere with a lower P, leads to higher $\delta^{13}C$ values in the atmosphere. Atmospheric $\Delta^{14}C$ increases with a slowing of P as the pathways for it to invade the ocean from its atmospheric source, are slower.

Net primary productivity (Fig. 4(p)) is a sink of CO_2, and also fractionates the carbon isotopes leading to increases in the atmosphere values. It is likely that NPP plays a dampening role and modulates CO_2, $\delta^{13}C$ and $\Delta^{14}C$ around the interglacial cycles (Toggweiler (2007)). Varying the ocean surface area volume (Fig. 4(q)) has modest impacts on CO_2 and $\delta^{13}C$, but a large impact on $\Delta^{14}C$. Decreasing the ocean volume leads to a lower surface area for atmospherically-produced radiocarbon to enter the ocean, causing it to build up in the atmosphere. Increasing the fraction of deep water upwelled into the sub polar box (Fig. 4(r)), intuitively raises CO_2 but lowers the values for the isotopes, as it increases the upwelling of carbon rich and isotopically-depleted water to the ocean surface boxes.

3.3 Modern carbon cycle simulation

Human fossil fuel and land-use change emissions have contributed ~575 Gt carbon to the atmosphere between 1751 and 2010 (Boden et al., 2017; Houghton, 2010) and up until 2014 were growing at an accelerating rate. The carbon cycle is not static in its response to the shocks, rather it continually partitions carbon between its component reservoirs amidst positive and negative feedbacks. Given the dominance of the human industrial emissions source in the modern global carbon cycle, a simulation model should be able to provide a plausible simulation of its effects. We model historical emissions data from 1751 and the IPCC's representative concentration pathway (RCPs) projections to 2100 to test the model's responses and compare with atmospheric data and published modelling results (e.g. CMIP5: https://cmip.llnl.gov/cmip5/). The experiment forces the late Holocene/preindustrial equilibrium with estimates of industrial fossil fuel and land use change CO_2 emissions and sea surface temperature (SST) changes, from historical data and the IPCC's RCP scenarios (Boden et al., 2017; Houghton, 2010; IPCC, 2013).

Figure 5 shows the modern carbon cycle simulation using SCP-M, compared with historical atmospheric data for CO_2, $\delta^{13}C$ and $\Delta^{14}C$ and GLODAPv2 ocean data (estimated data year 1990). Importantly, SCP-M provides an accurate simulation of the carbon cycle response to the human emissions inputs by replicating the atmospheric patterns for CO_2, $\delta^{13}C$ and $\Delta^{14}C$ preserved in data observations for the period 1751-2016 (a-b). The atmospheric CO_2 and $\delta^{13}C$ data is sourced from the Scripps CO_2 program (originally sourced from http://scrippsco2.ucsd.edu, data currently being transitioned to http://cdiac.ess-dive.lbl.gov), and $\Delta^{14}C$ data is sourced from Stuiver et al. (1998) and Turnbull et al. (2016). A key feature of the historical data is the substantial uplift in human emissions from circa 1950 onwards which is accompanied by an uplift in atmospheric CO_2 and a steep drop in $\delta^{13}C$ (Fig. 5(a)). The latter reflects the $\delta^{13}C$-depleted human emissions. The emissions effect on atmospheric $\Delta^{14}C$ (Fig. 5(b)) in the 20th century is largely overprinted by the effects of bomb radiocarbon. The effect of emissions is seen as a slight downturn in the model and data $\Delta^{14}C$ in the immediate lead up to the release of bomb radiocarbon into the

atmosphere, and then resumes downward from ∼2020. The spike in $\Delta^{14}C$ during the period of bomb radiocarbon release, lasts during the period 1954-1963 and then quickly disperses as 14C is absorbed by the ocean. The simulation shows that SCP-M is also in good agreement with the GLODAPv2 ocean data by 1990 (Fig. 5(c-f)), with most boxes falling within the standard deviation of average data values, lending confidence to the model's simulation of carbon redistributive processes. Figure 6

5   shows the emissions profile (a) and modelling results (b) for atmospheric CO_2 over historical time and projected forward to 2100 for the IPCC RCPs. The SCP-M output undershoots the IPCC projections for RCP 2.6 and 4.5, but provides a close match on RCP 6.0 and 8.5.

    Figure 7(a) shows the the annual uptake of CO_2 by the ocean. The model begins the period close to a steady state between the atmosphere and surface ocean pCO_2, with limited transfer across the interface. Beginning circa 1950 the ocean begins to

10   take up an increased load of CO_2 from the atmosphere. By 2100, SCP-M models a range of annual CO_2 uptake by the ocean of 0-6 PgC annum^{-1} across the RCPs. This is similar to the range of values estimated by the CMIP5 models as shown in Fig. 7(a), reproduced from Jones et al. (2013). The cumulative uptake of emissions by the ocean over the period 1751-2100 (Fig. 7(b)) modelled by SCP-M of ∼350-750 PgC, is at the upper end of the modelled range of CMIP5 models of ∼200-600 PgC over the period 1850-2100 (Jones et al., 2013). The SCP-M simulations commence in 1751 and therefore incorporate an extra

15   100 years of fossil fuel and land use change emissions beyond the CMIP5 model results presented in Jones et al. (2013). Wang et al. (2016) quote a range of 412-649 PgC cumulative uptake by the ocean by 2100 from 11 CMIP5 models, a closer range to the SCP-M outcomes. Figure 8 shows the carbon cycle destination for human emissions by 2100, in the SCP-M simulation. By 2100 the load of human emissions is roughly 40:60 split between the atmosphere and the combined terrestrial biosphere and ocean. The terrestrial biosphere portion of the pie chart shows only the CO_2 sink behaviour, gross of deforestation emissions

20   which reduce the terrestrial carbon stock and are subsequently taken up by all of the carbon reservoirs.

    By 2100 in RCP 6.0, the carbon cycle is substantially changed from the preindustrial/late Holocene state by the sustained release of human emissions over hundreds of years (Fig. 9). The release of emissions transfers carbon to the atmosphere, ocean and terrestrial biosphere. The flux behaviours also change. In the preindustrial state, CO_2 enters the ocean in the low latitudes and northern ocean (shown as negative fluxes in Fig. 9), and de-gasses in the Southern Ocean (positive flux) under

25   the influence of ocean upwelling in that region. In the RCP 6.0, the atmospheric CO_2 concentration increases to the extent that the atmosphere-ocean pCO_2 gradient drives all surface ocean boxes to take carbon from the atmosphere, despite simulated warmer surface ocean temperatures towards the end of the projection. The terrestrial biosphere influx of carbon is dramatically increased by the carbon fertilisation effect, leading to a larger biomass stock which in turn also causes more respiration - both inward and outward biosphere fluxes of CO_2 are therefore greatly enhanced. The weathering of silicate rocks on the

30   continents, a weak sink of carbon, also accelerates under the effects of burgeoning atmospheric CO_2, transferring carbon from the atmosphere to the ocean via rivers. The physical fluxes of carbon within the ocean are only modestly affected, with the main exception being low latitude thermocline mixing, which in the RCP 6.0 mixes a larger amount of carbon back into the surface ocean box from intermediate depths. The altered balance of DIC:alkalinity, particularly in the abyssal box, leads to a decrease in the carbonate ion concentration of abyssal waters, late in the projection period, which in turn causes more dissolution of

35   marine sediments. By 2100 this feedback brings more carbon back into the ocean, increased from 0.2 to 1.1 PgC yr^{-1}, but also
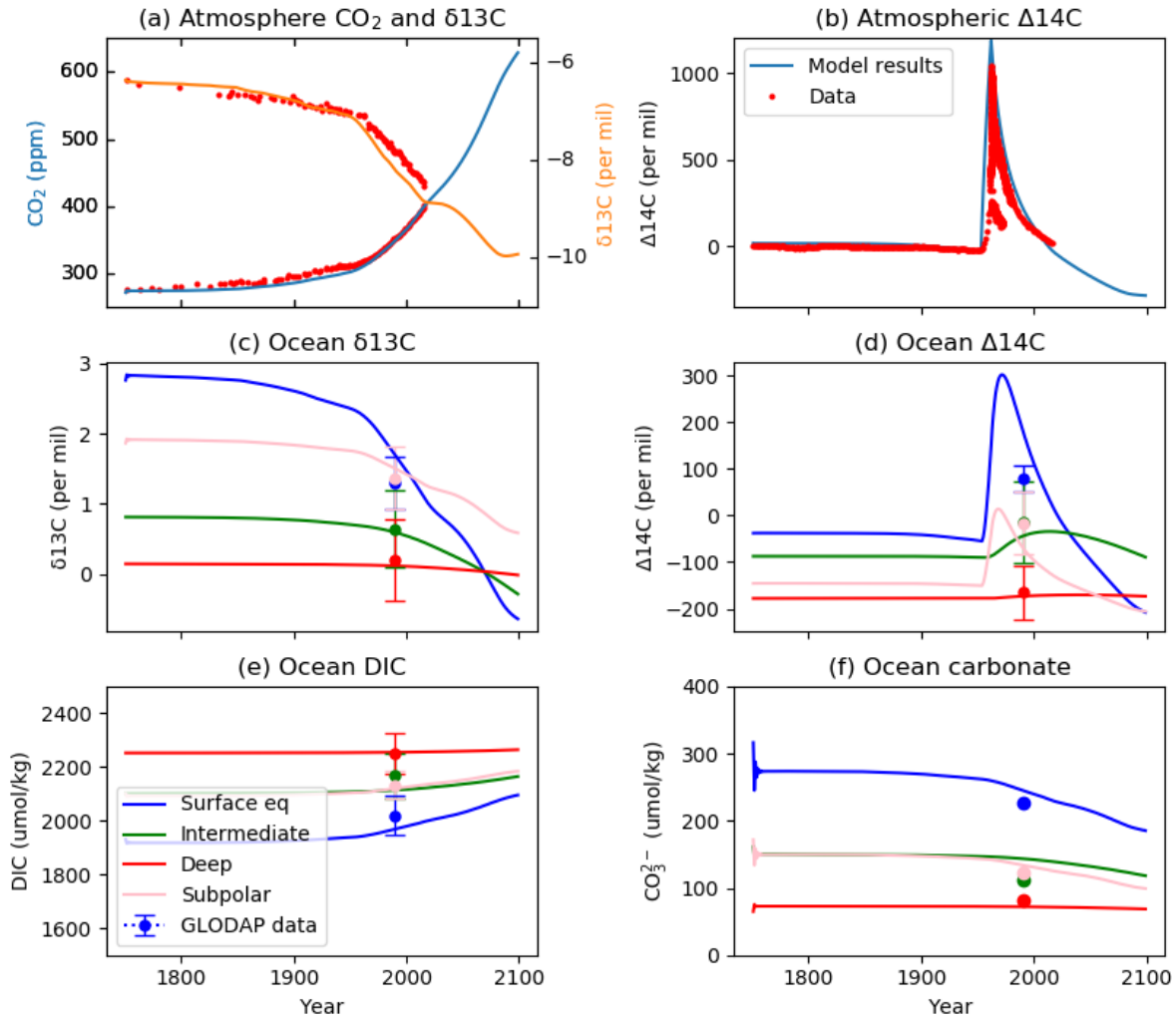
Figure 5. SCP-M modelling results compared with modern atmospheric and ocean GLODAPv2 data. Selection of boxes shown to reduce clutter. Projections beyond 2015 include RCP 6.0 emissions growth. In the top row we plot SCP-M model results for CO_2, $\delta^{13}C$ and $\Delta^{14}C$ (lines) for the period 1751-2100 against atmospheric data for CO_2, $\delta^{13}C$ and $\Delta^{14}C$ (red dots). The SCP-M model output closely resembles the atmospheric data record. The perturbation from industrial-era, isotopically depleted ($\delta^{13}C$) and dead ($\Delta^{14}C$) CO_2 is clear, as is the impact of atmospheric nuclear tests on $\Delta^{14}C$ during 1954-1963. In the other rows we plot SCP-M model results (boxes as shown) versus GLODAPv2 data (dots/error bars, same colour as corresponding boxes). We assume an average data year of 1990 for the GLODAPv2 data accumulated over the period 1972-2013. For most of the SCP-M ocean boxes, the model results fall within or very close to error ranges of the GLODAPv2 data, despite large perturbations in the model and data from industrial-era emissions and bomb radiocarbon.
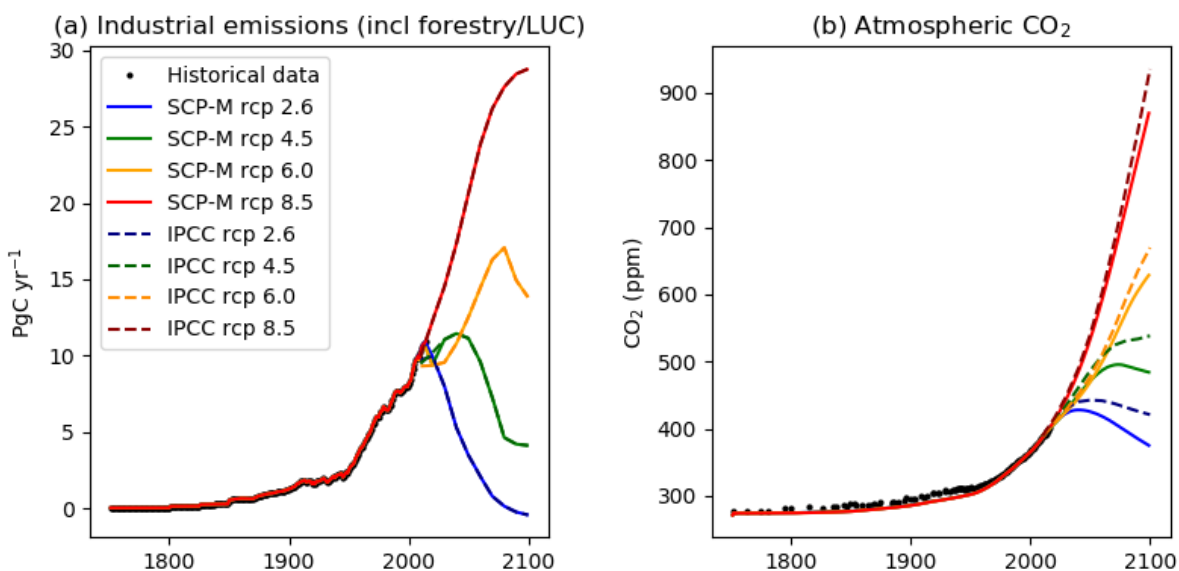
Figure 6. RCP Modelling results compared with IPCC emissions and CO_2 scenarios. Panel (a) shows the IPCC's RCP emissions pathways out to 2100 which are fed into SCP-M for the modern carbon cycle simulation. Panel (b) shows SCP-M model output for atmospheric CO_2 plotted against IPCC atmospheric CO_2 projections for the RCP pathways. The SCP-M output undershoots the IPCC projections for RCP 2.6 and 4.5, but provides a close match on RCP 6.0 and 8.5.

alkalinity (in a ratio of 2:1 to DIC), thereby serving to lower whole of ocean pCO_2 - a modest negative feedback. In summary, SCP-M provides an accurate simulation of historical atmospheric CO_2, $\delta^{13}C$ and $\Delta^{14}C$ data, when forced with anthropogenic CO_2 emissions data over the same period. For the forward-looking RCP emissions projections, SCP-M falls in the range of the CMIP5 models, although the oceanic carbon uptake is exaggerated for the RCP 8.5 scenario. This suggests that a more detailed

5   experiment, for example with non-linear representation of the piston velocity with respect to atmospheric CO_2, might provide a closer fit to the CMIP5 models.

4   LGM-Holocene model-data experiment

The settings for global carbon cycle flux parameters on paleo, interglacial timeframes, remain unresolved (Sigman et al., 2010). The LGM-Holocene dilemma, in particular, looms large in paleoceanography. To date, a precise set of physical changes to

10   account for the large end-of-glacial carbon cycle changes, remains elusive (e.g. Menviel et al., 2016). In the modelling context, this problem traditionally related to uncertainty over the values of key parameters, such as ocean circulation or biology, to use in LGM and late Holocene simulations, and use of models to manually test hypothesis inputs. Conversely, constraints on the parameter values derived from modelling, can perhaps equally usefully serve as a constraint on candidate hypotheses.
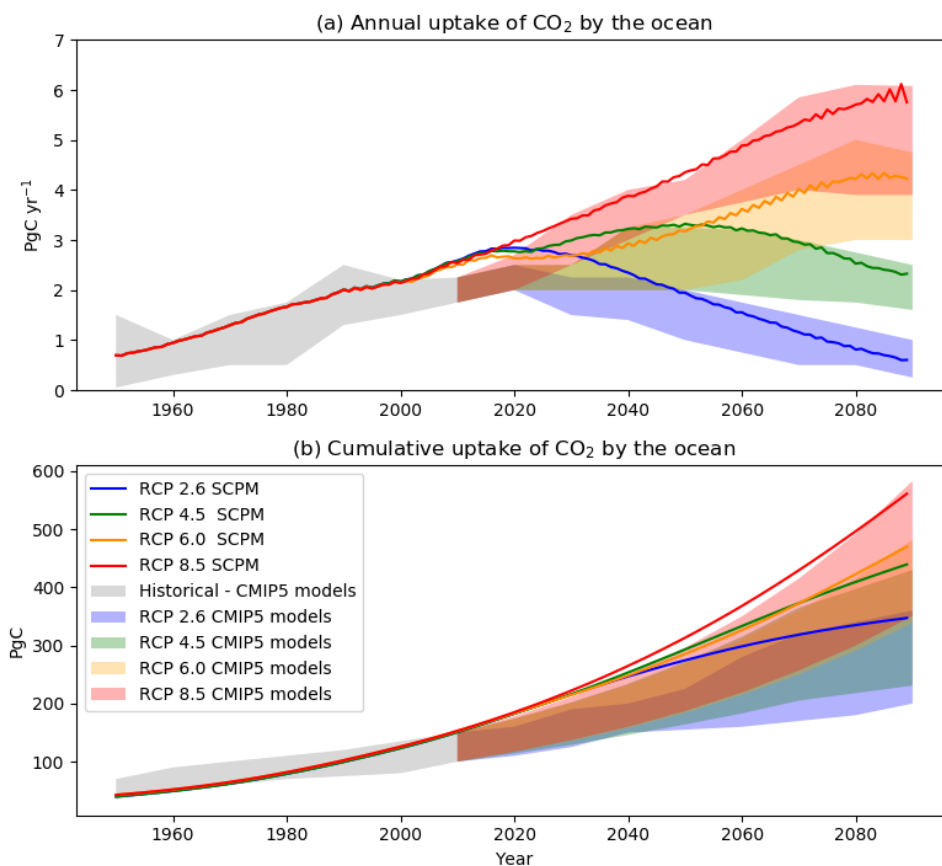
Figure 7. Panel (a) shows shows the annual uptake of CO_2 by the ocean in each of the RCP's over the period 1751-2100, modelled with SCP-M. By 2100, SCP-M estimates a range of 0-6 PgC year^{-1} across the RCPs as estimated by CMIP5 models, reproduced from Jones et al. (2013). Panel (b) shows the cumulative uptake of CO_2 by the ocean over the same period modelled with SCP-M and compared with CMIP5 models (Jones et al., 2013).

To this end, we illustrate SCP-M's capabilities by solving for the parameter values of best-fit with late Holocene and LGM ocean and atmosphere proxy data, using a model results-data optimisation. For this illustrative example, the ocean data is taken from published sources (Table 1), averaged for the LGM (∼18-24 ka) and Late Holocene (6.0-0.2 ka) time periods and for box coordinates (depth and latitude), and the mean and variance for each box average is then calculated. Where necessary, we

5 undertook additional spreadsheet-processing of radiocarbon data to yield the all-important $\Delta^{14}C$ values, which incorporates the independent calendar-age and corrects for biological fractionation (Fallon, 2018).

First, we probe the potential for key model parameters to drive Holocene-LGM changes in atmospheric carbon variables, to focus our experiment on these parameters. It is likely that the LGM to Holocene carbon cycle changes were dominated by the ocean (Sigman and Boyle, 2000), but were also accompanied by a range of physical changes in the atmosphere and
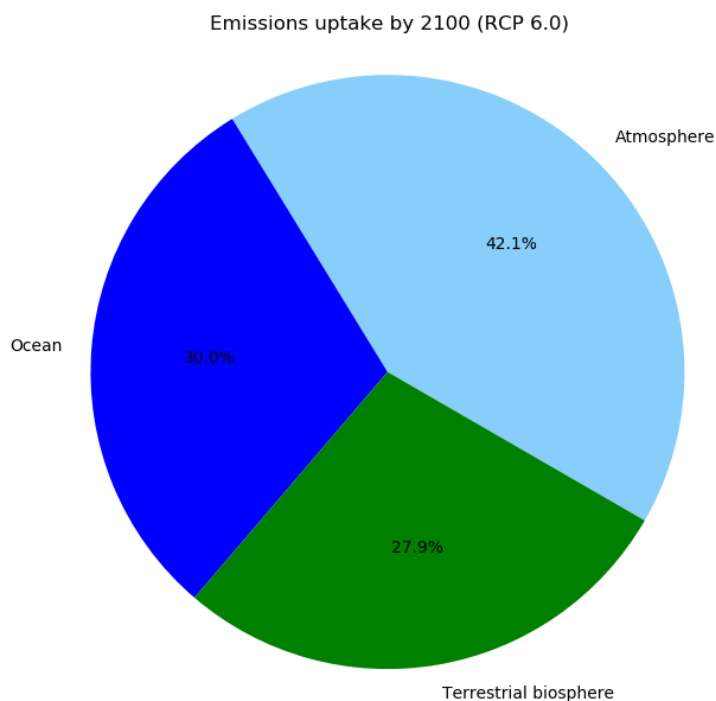
Figure 8. Relative uptake of CO_2 across the major carbon reservoirs by 2100 in the RCP 6.0 as modelled by SCP-M. By 2100, SCP-M projects that 42% of industrial-era emissions remain in the atmosphere, 30% reside in the ocean and 28% in the atmosphere.

terrestrial biosphere that in aggregate, could be material (e.g. Sigman and Boyle, 2000; Adkins et al., 2002; Ferrari et al., 2014). These changes include sea surface temperature, salinity, sea-ice cover, ocean volume and atmospheric 14C production rate. Estimates of average sea surface temperature for the LGM generally fall in the range of 3-8°C cooler than the present (Trent-Staid and Prell, 2002; Annan and Hargreaves, 2013). Adkins et al. (2002) estimated ocean salinity was 1-2 psu higher

5   in the LGM and sea levels were ∼120m lower (Adkins et al., 2002; Grant et al., 2014). Stephens and Keeling (2000) and Ferrari et al. (2014) highlighted the role of expanded sea ice cover in the Southern Ocean during the LGM as a key part of the LGM CO_2 drawdown. Finally, Mariotti et al. (2013) estimated that higher atmospheric radiocarbon production accounted for +∼200‰ in atmospheric $\Delta^{14}C$ in the LGM. Mariotti et al. (2013) simulated this variation in model experiments by increasing the radiocarbon production rate by a multiple of 1.15-1.30 (best guess 1.25) of the modern estimate in order to recreate LGM

10    $\Delta^{14}C$ values. Using these findings we define two background states for modelling purposes: a late Holocene state (as per our
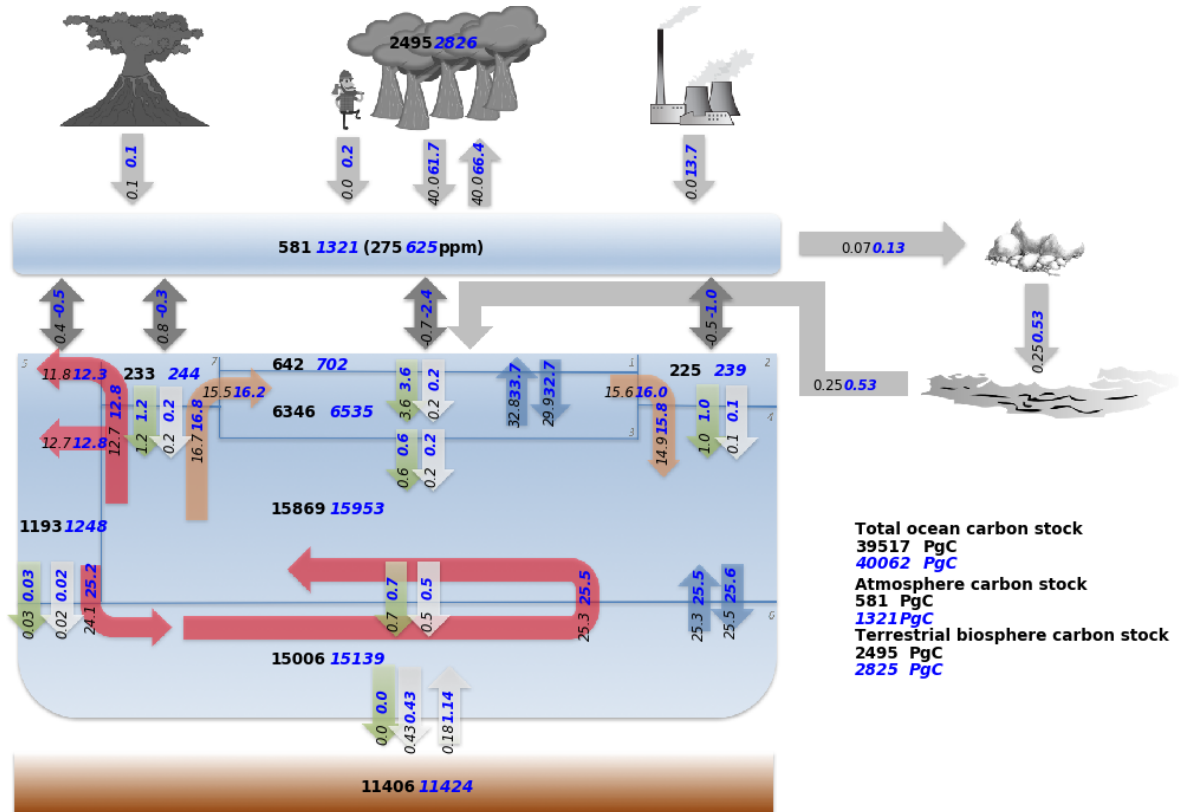
Figure 9. SCPM-modelled preindustrial carbon stocks and fluxes (in black text) compared with IPCC RCP 6.0 emissions scenario by 2100 (in blue text). Atmosphere, ocean and terrestrial biosphere take up the load of carbon from the industrial source. By 2100, carbon is fluxing into all ocean boxes, the terrestrial biosphere and continental sediment weathering/river fluxes. Preindustrial outgassing of CO_2 in the Southern Ocean is reversed, and carbon is returned to the ocean via enhanced $CaCO_3$ dissolution. Box numbers on the diagram refer to ocean regions specified in Fig. 1. Negative fluxes on bidirectional arrows are fluxes of CO_2 out of the atmosphere.

starting data and literature foundations in Table 4) and the LGM state, as per the hypothesised changes in temperature, sea surface area, sea ice cover and salinity (Table 2).

Indicator	LGM change
Surface ocean box temperatures	-5-6°C (Trent-Staid and Prell, 2002; Annan and Hargreaves, 2013)
Surface ocean box salinity	+1.0 psu (Adkins et al., 2002)
Polar ocean box piston velocity	x0.3 (Stephens and Keeling, 2000; Ferrari et al., 2014)
Ocean surface area and volume	-3.0% (Adkins et al., 2002; Grant et al., 2014)
Atmosphere radiocarbon production	x1.25 (Mariotti et al., 2013)

Table 2. Changes to ocean and atmosphere parameter settings in SCP-M to recreate the LGM background model state. As shown in the sensitivity tests in Fig. 4, some processes do not exert a strong influence on atmospheric CO_2, but do impact modestly on CO_2 and strongly on $\delta^{13}C$ and $\Delta^{14}C$. Where these features are posited to vary around glacial cycles, we have incorporated them as a step change from late Holocene/modern estimates, in our LGM model experiment

Figure 10 shows the cumulative effect of these changes in SCP-M, within the late Holocene-LGM atmosphere 3D CO_2-$\delta^{13}C$-$\Delta^{14}C$ data space. These changes are the first stage of a model adjustment to analyse the potential for ocean circulation and biological changes to deliver the LGM atmospheric CO_2, $\delta^{13}C$ and $\Delta^{14}C$ values, and take the model output from the red circle (Late Holocene) to the black star. The decrease in ocean surface box temperatures leads to a drop in CO_2 of ∼20 ppm and a lightening of $\delta^{13}C$ by ∼0.6‰, owing to the increased solubility of CO_2 in colder water, and the increasing fractionation of $\delta^{13}C$ with decreasing temperatures, which leaves more ^{12}C in the atmosphere. There is limited impact on $\Delta^{14}C$. Increasing salinity slightly reverses these changes to CO_2 and $\delta^{13}C$. Reducing sea surface area and volume slightly increases CO_2 and $\Delta^{14}C$ as the ocean's capacity to take up these elements is reduced. Slowing down the piston velocity in the polar Southern Ocean box, as a proxy for increased sea ice cover, slightly reduces CO_2 (reduced outgassing), increases $\Delta^{14}C$ (slower rate of invasion to the ocean) and increases $\delta^{13}C$ as the de-gassing sea-to-air fractionation of $\delta^{13}C$ is reduced. Finally, increasing the rate of atmospheric radiocarbon production creates a shift in $\Delta^{14}C$ (horizontal shift in Fig. 10) towards the LGM levels (black circle in Fig. 10). In aggregate, these changes lead to a fall in CO_2 of ∼35 ppm, a fall in $\delta^{13}C$ of ∼-0.5‰ and an increase in $\Delta^{14}C$ of ∼300‰.

From the black star in Fig. 10, the "LGM state", we perform a focussed sensitivity test on key hypothesised drivers of LGM-Holocene carbon cycle changes (Sigman et al., 2010). These are: slower global overturning circulation (Ψ_1), slower AMOC (Ψ_2), reduced deep-abyssal ocean mixing (γ_1) and a stronger biological pump (Z). The Z biology parameter, varied across 5-10 mol C m^{-2} yr^{-1}, can deliver the LGM CO_2 changes, but steers $\delta^{13}C$ and $\Delta^{14}C$ away from their LGM values. γ_1 drives ancillary changes in all three variables, suggesting it is not the driver of the LGM atmospheric changes but may play a modulating role. Both Ψ_1 (3-29 Sv) and Ψ_2 (3-19 Sv) experiments run very close to the LGM data values on their own, although neither can deliver a precise hit.
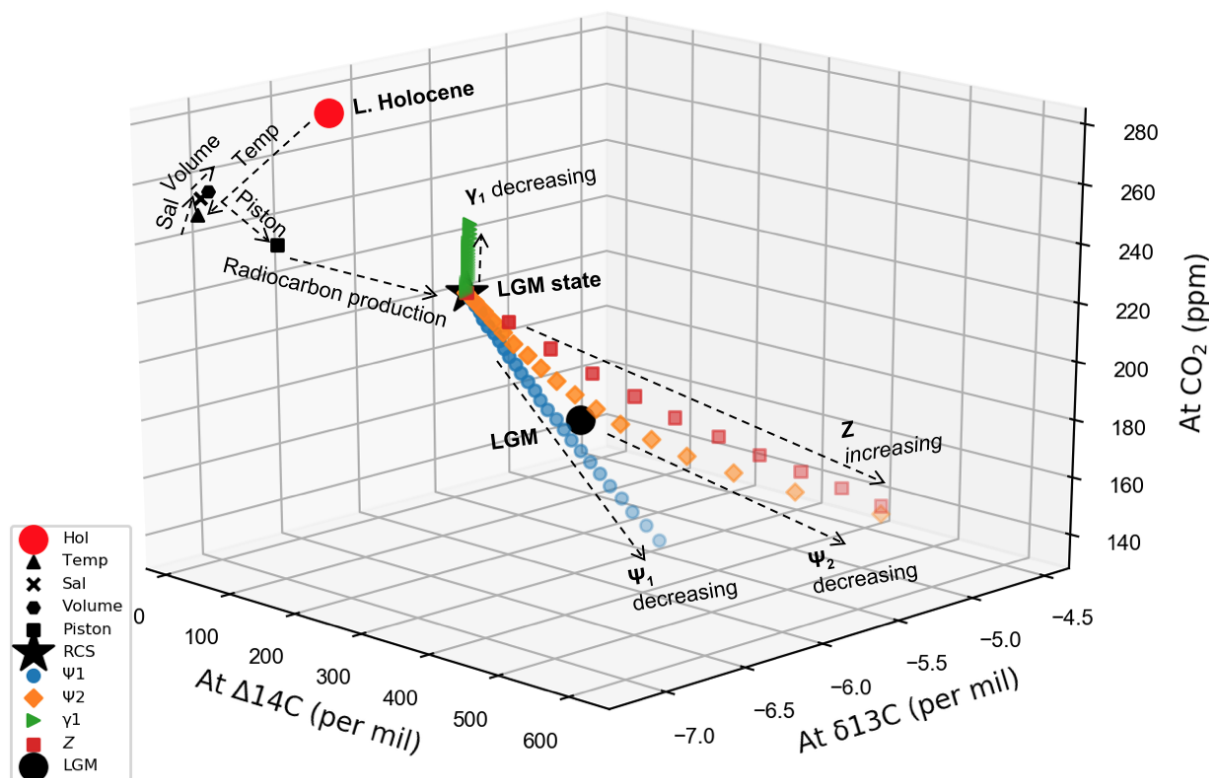
Figure 10. LGM state parameter adjustments. Using the posited LGM changes in environmental parameters in Table 2, we establish the LGM foundations for exploring the impacts of varying large scale ocean process parameters towards LGM atmospheric CO_2-δ^{13}C-Δ^{14}C data space. The red circle is our starting point for the late Holocene. From the LGM state foundation (black star), variation of global overturning circulation (Ψ_1), Atlantic meridional overturning circulation (Ψ_2) and the soft-tissue biological pump (Z), drives atmospheric CO_2, δ^{13}C and Δ^{14}C into the vicinity of their LGM data values (black circle). The biological pump Z can effect the LGM CO_2 outcome, but steers δ^{13}C away from the LGM value. Both Ψ_1 (3-29 Sv) and Ψ_2 (3-19 Sv) experiments run very close to the LGM data values on their own, although neither can deliver a precise hit

Using the literature-referenced Holocene and LGM background parameter states, and informed by the sensitivity analysis in Fig. 10, we take advantage of the model's fast run time to perform thousands of multi-variant simulations over the free-floating Ψ_1, Ψ_2, γ_1 and Z parameter spaces, and perform an optimisation routine against the data for each data period. The SCP-M script harvests model results and performs a least squares data-results optimisation against the LGM and late Holocene data for

Parameter (units)	Data values L. Holocene (LGM)	Late Holocene experiment results	LGM experiment results
Ψ_1 (Sv)	20-30 (na)	**29**	**17**
Ψ_2 (Sv)	15-25 (na)	**19**	**16**
γ_1 (Sv)	na (na)	**29**	**25**
Z (mol C m^{-2} yr^{-1})	2-10 (na)	**5**	**5**
At CO_2 (ppm)	275±6 (195±3)	275	197
At $\delta^{13}C$ (‰)	-6.35±0.09 (-6.46±0.01)	-6.35	-6.46
At $\Delta^{14}C$ (‰)	20±48 (414±32)	21	400

Table 3. Late Holocene and LGM model-data parameter optimisation and associated atmospheric variable model output. Bold font parameter results indicate those parameters that are free-floating and determined by the model and data in the experiment. The LGM experiment show a marked decline in the strength of global overturning circulation Ψ_1 (-12 Sv), and a modest decline in Atlantic meridional overturning circulation Ψ_2 to deliver the LGM atmosphere and ocean data signal. A modest decline in deep-abyssal mixing γ_1 is also seen

atmospheric CO_2, atmospheric and ocean $\Delta^{14}C$ and $\delta^{13}C$, and also oceanic carbonate ion proxy, to source the best parameter values for Ψ_1, Ψ_2, γ_1 and Z (or any parameter specified):

$$Opt_{n=1} = Min \sum_{i,k=1}^{N} (\frac{R_{i,k} - D_{i,k}}{\sigma_{i,k}})^2 \tag{24}$$

where: $Opt_{n=1}$ = optimal value of parameters n, $R_{i,k}$ = model output for concentration of each element i in box k, $D_{i,k}$ =
5   average data concentration each element i in box k and $\sigma_{i,k}$ = standard deviation of the data for each element i in box k. The standard deviation performs two roles. It reduces the weighting of a variable with an uncertain value and also normalises for the different unit scales (e.g. ppm, ‰ and umol kg^{-1}), which allows multiple proxies in different units to be incorporated in the optimisation. Where data is unavailable for a box, that element and box combination is automatically nulled from the optimisation routine.

10   The late Holocene data-optimised results show good agreement with the Talley (2013) observations for Ψ_1 (29 Sv) and Ψ_2 (19 Sv) from the the modern ocean (Table 3). The starting base value of Z, of 5 mol C m^{-2} yr^{-1}, is returned in the experiment. The experiment also successfully returns values for atmospheric CO_2, $\delta^{13}C$ and $\Delta^{14}C$ within standard error for the late Holocene data series.

15   The ocean and atmosphere model results for the LGM (bold stars) and late Holocene (transparent stars) experiments using the optimised parameter settings in Table 3, are plotted in Fig. 11 along with the corresponding data (blue dots with error bars for standard deviation). The experiment provides results within the error bounds of data for most of the box regions in both scenarios, and an excellent fit to the change in the relative distribution of the proxies between ocean boxes and the atmosphere
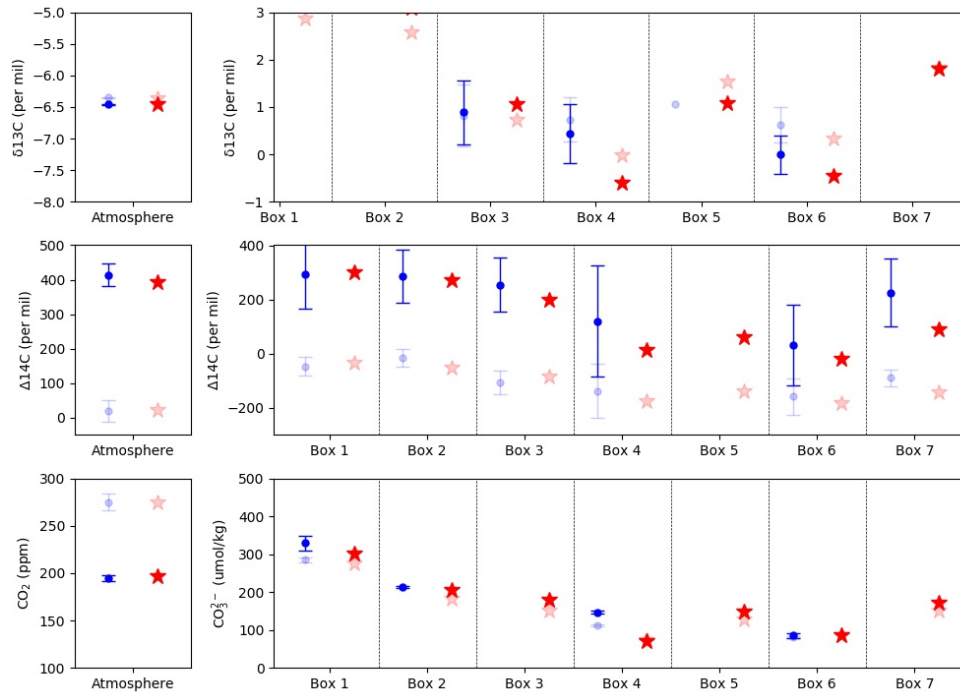
Figure 11. LGM atmosphere and ocean data-optimised model results. Left panels shows the atmospheric carbon cycle results (red stars) plotted against LGM average data values (blue dots) with standard error bars. The right panel shows the ocean results plotted against LGM average ocean data where available. Corresponding Holocene data and results shown with transparent markers. The data-optimised model results show a close match for the LGM atmospheric data and most of the ocean data. The ocean δ^{13}C and Δ^{14}C data show an increased compositional gradient between shallow-intermediate depths (boxes 1-3) and deep-abyssal depths (boxes 4 and 6), an outcome effected in the corresponding model results mainly by a slower global overturning circulation. Data sources are shown in Table 1.

which is preserved in the LGM and late Holocene data. A key feature of the ocean δ^{13}C data is a depletion of deep ocean δ^{13}C in the LGM, shown as a drop in δ^{13}C values in the deep (box 4) and abyssal (box 6) boxes, relative to the intermediate box (3). In the LGM δ^{13}C data, there is a spread of 1‰ across these water masses, which narrows to 0.3‰ in the late Holocene data. The pattern is replicated in the LGM model experiment, pointing to the important role of changes in abyssal-deep ocean water

5   flows, via Ψ_1, in delivering the ocean δ^{13}C data patterns. The model shift in δ^{13}C in the deep box (box 4) of 0.6‰ from the LGM to late Holocene, is in good agreement with a global deepwater estimate of 0.49 $\pm$0.23‰ by Gebbie et al. (2015) and an earlier estimate of 0.46‰ by Curry et al. (1988). The average atmospheric δ^{13}C value remains largely unchanged between the two periods, due to the δ^{13}C-buffering effect of the terrestrial biosphere which takes up CO_2 in the Holocene period (increases atmospheric δ^{13}C), and respires CO_2 in the LGM period (decreases atmospheric δ^{13}C).

10   The model results also closely replicate the reduction in deep-to-shallow ocean compositional gradient in Δ^{14}C data moving from the LGM to Holocene period (e.g. Skinner and Shackleton, 2004; Skinner et al., 2010; Burke and Robinson, 2012; Skinner

et al., 2015; Chen et al., 2015; Hines et al., 2015; Ronge et al., 2016). The LGM data shows a spread of $\sim$300‰ between abyssal (box 6) and intermediate (box 3) waters, and deep (box 4) versus surface (boxes 1, 2 and 7) boxes. In the Holocene data, the spread is narrowed to $\sim$100‰. This data observation was popularly characterised as the result of increased Southern Ocean upwelling of Δ^{14}C-depleted deep water into intermediate and shallow depths in the Holocene (e.g. Skinner et al., 2010; Burke

5 and Robinson, 2012; Skinner et al., 2015). A slow-down in Southern Ocean upwelling in the LGM allows Δ^{14}C-depleted water to accumulate in the deep or abyssal ocean and a widening in the Δ^{14}C gradient between deep and shallow waters. In SCP-M, this is simulated by lower values for Ψ_1 and Ψ_2. The low latitude surface box (box 1) enrichment in Δ^{14}C in planktonic foraminifera in the LGM, is replicated by the increased atmospheric production rate of radiocarbon applied to the LGM experiment, combined with slower ocean circulation.

10 Carbonate ion proxy data coverage is sparse, however SCP-M results are shown for comparison against the data that is available. The model results for the carbonate ion proxy mirror the limited variation in the data between the LGM and Holocene. The changes are most pronounced in the surface boxes (boxes 1 and 2), which are under the influence of atmospheric CO_2, and attenuate somewhat in the deeper boxes (boxes 4 and 6). Yu et al. (2014b) interpreted the relatively small changes in carbonate ion in the deepest ocean (box 6) as the result of efficient buffering of deep water pH by carbonate dissolution, most notably in

15 the Pacific Ocean. The model result for the deep box (box 4) goes against the LGM-Holocene variation in the data, but given there is only one data point for this part of the ocean, and the variation itself is small, it is an uncertain outcome.

The LGM scenario shows important changes in the carbon redistributive behaviour of the ocean (Fig. 12). The stock of carbon increases in abyssal and deep boxes, and reduces in the intermediate, low latitude surface and northern surface boxes. The amount of carbon upwelled to the sub polar surface box by the global overturning circulation (Ψ_1), drops by $\sim$ 5-10

20 PgC yr^{-1}, with the most pronounced changes taking place at the abyssal-deep box boundary. The slower upwelling rate of carbon causes a reduced outgassing rate of CO_2 from the sub polar box to the atmosphere. The weaker flux of Ψ_2 also brings a reduced DIC load into the intermediate depth ocean, the driver for lower DIC content in the intermediate and surface boxes. The optimised parameter run for the late Holocene results in a terrestrial biosphere carbon pool of 2,495 Pg C, which is fortuitously close to the preindustrial estimate of Raupach et al. (2011) (2,496 Pg C), at the top end of acceptable values in Francois et al.

25 (1999), and close to the "active" land carbon pool of 2,370 $\pm$ 125 estimated by Ciais et al. (2012). In the optimised LGM model results, the terrestrial biosphere is reduced to 1,828 Pg C, a differential of 667 Pg C between the two periods, which is towards the upper bound of recent estimates of the delta (0 - 700 Pg C e.g. Ciais et al. (2012), Peterson et al. (2014)), but within uncertainty bounds. For example, Peterson et al. (2014) estimated a variation of 511 $\pm$ 289 Pg C in the terrestrial biosphere carbon stock based on whole of ocean δ^{13}C data, the same data used in this exercise. According to Francois et al.

30 (1999), palynological and sedimentological data showed deltas in the range of 700 to 1350 Pg C. Ciais et al. (2012) pointed to a growth of a large inert carbon pool in steppes and tundra during the LGM, which may have modulated some of the active biosphere carbon signal, a factor not explicitly covered in our modelling exercise. The terrestrial biosphere is clearly a key part of the carbon cycle transition. The atmosphere-enriching fractionation of δ^{13}C by the terrestrial biosphere during the deglacial period, effectively reverses the effects of the release of δ^{13}C-depleted carbon from the deep ocean to the atmosphere at the

35 termination and leaves atmosphere δ^{13}C almost unchanged from LGM values as a result (Schmitt et al., 2012). The DIC:Alk

balances in the abyssal ocean during the LGM also drive subtle changes in the balance of carbonate out-flux by sinking and influx from sediment dissolution, which build up to substantial differences in the sediment carbon stock between the LGM and Holocene simulations, mainly due to the timeframes modelled in the SCPM spin-up for each scenario (15 kyr).

The model-data results using SCP-M and published data suggest that variations in the strength of the large scale ocean

5   physical processes, particularly the global overturning circulation, can account for the LGM to Holocene carbon cycle changes inferred in the proxy data, but critically accompanied by a number of ancillary processes. Importantly, this result is observed on account of ocean and atmosphere data, across CO_2, $\delta^{13}C$, $\Delta^{14}C$ and carbonate ion proxy. Talley (2013), re-emphasised the importance of the Pacific Ocean overturning circulation limb in the global overturning circulation, which implies it is an important part of the global carbon cycle alongside the Atlantic Ocean, a finding corroborated by Skinner et al. (2017) in

10 a recent review of Pacific Ocean radiocarbon data. The data-model results using SCP-M suggest that the global overturning circulation was reduced during the LGM, accompanying enhanced storage of isotopically-depleted carbon in the abyssal and deep ocean from atmospheric and terrestrial biosphere sources. There is support for such a composite mechanism involving a number of physical changes alongside an oceanic driver (e.g. Sigman et al., 2010; Hain et al., 2010; Ferrari et al., 2014; Menviel et al., 2016).

15 **5   Conclusions**

The SCP-M carbon cycle box model was constructed for the purposes of scenario or hypothesis testing (quickly and easily), data-model integration and inversion, paleo reconstructions, and analysing the distribution of anthropogenic emissions in the carbon cycle. The model contains a full ocean-atmosphere-terrestrial carbon cycle with a realistic treatment of ocean processes. Despite being relatively simple in concept and construct, SCP-M can account for a range of paleo and modern carbon cycle

20 observations. The model applications illustrated here include integration with datasets from the present day (GLODAP, IPCC) and ocean paleo proxy data across the LGM and late Holocene periods. Simulations of the modern carbon cycle indicate that SCP-M provides a realistic representation of the dynamic shocks from human industrial and lad use change emissions and bomb 14C. A model-data experiment using LGM and Holocene CO_2, $\delta^{13}C$, $\Delta^{14}C$ and carbonate ion proxy, is able to resolve parameter values for ocean circulation, mixing and biology while reproducing model results that are very close to the proxy

25 data for both time periods. The experiment results indicate that the LGM to Holocene carbon cycle transition can be wholly explained by variations in the strength of global overturning circulation and Atlantic meridional overturning circulation, when combined with a number of background changes such as sea surface temperature, salinity, sea-ice cover, ocean volume and a varied atmospheric radiocarbon production rate. Further work on data quality and analysis is required to validate this finding, which is the subject of a separate paper. The results show promise in helping to resolve the LGM to Holocene carbon cycle

30 dilemma and point towards an ongoing application for data-constrained models such as SCP-M.
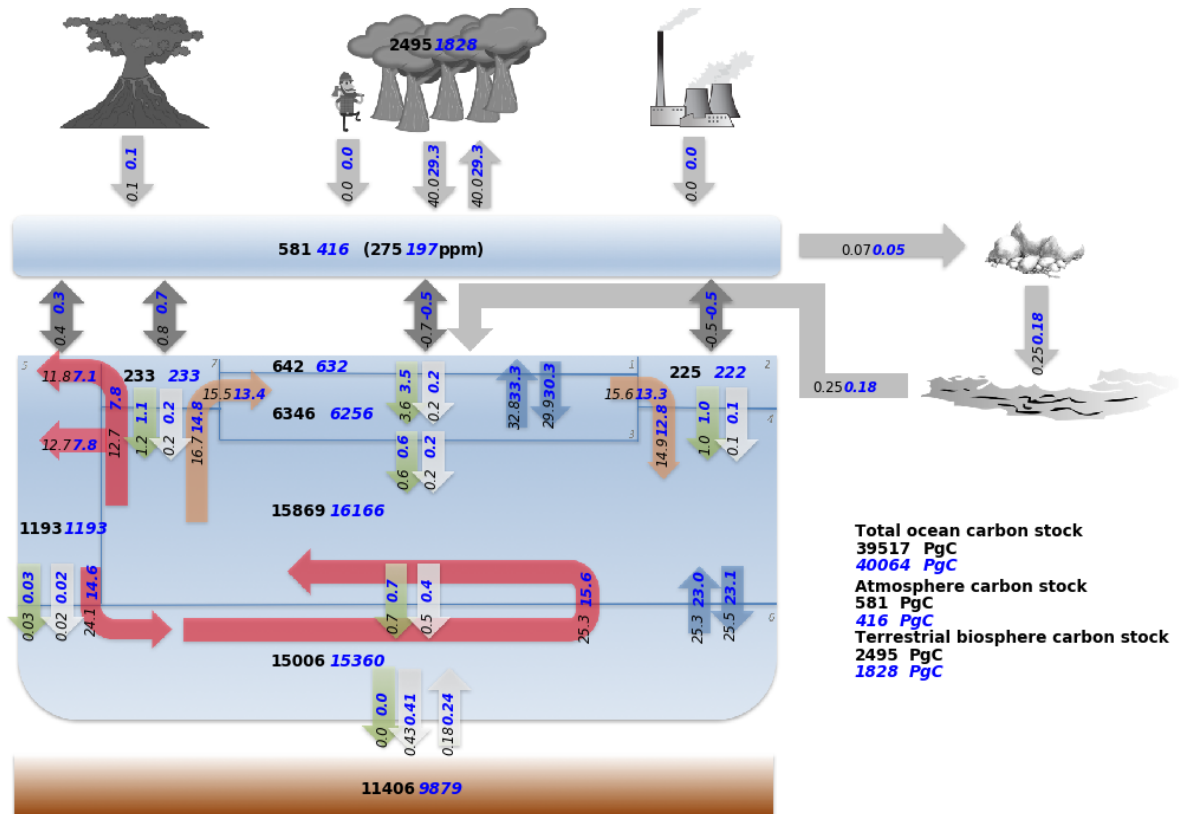
Figure 12. Late Holocene (figures in black text) and LGM (blue text) carbon stocks and fluxes modelled with SCP-M. LGM parameter values selected from the 4 parameter LGM experiment in Table 3. The LGM setting leads to a transfer of carbon from the atmosphere and terrestrial biosphere to the deep ocean. Carbon upwelled into the surface ocean falls, leading to reduced outgassing of CO_2 in the Southern Ocean boxes. Continental weathering and river fluxes of carbon are also reduced due to lower atmospheric CO_2, leading to a change in amount of $CaCO_3$ burial and dissolution in marine sediments until equilibrium is restored with river input to the oceans. Box numbers on the diagram refer to ocean regions specified in Fig. 1.

6 Code availability

The full model code and all file dependencies, with user instructions are located at: https://doi.org/10.5281/zenodo.1310161

7 Data availability

No original geochemical data was created in the course of the study, but any data used necessary to run the model is located
5 with the model code at: https://doi.org/10.5281/zenodo.1310161

Appendix A

A1 Treatment of carbon isotopes

Carbon isotopes are an important component in the model given they are key sources of proxy data. The carbon isotopes are
treated largely the same as carbon in terms of fluxes in the model, with some modification. For example, carbon isotopes are
10 typically reported in delta notation (δ^{13}C and Δ^{14}C), which is the ‰ deviation from a standard reference value in nature. The
model operates with a metric mol m^{-3} for ocean element concentrations and flux parameters. In order to incorporate δ^{13}C and
Δ^{14}C into this metric for the operation of model fluxes, the method of Craig (1969) is applied to convert starting data values
of δ^{13}C and Δ^{14}C from delta notation in ‰, into mol m^{-3}:

$$^{13}C_i = (\frac{\delta 13 C_i}{1000} + 1)RC_i \tag{A1}$$

15 Where $^{13}C_i$ is the ^{13}C concentration in box i in mol m^{-3}, δ^{13}C$_i$ is δ^{13}C in ‰ in box i, R is the $\frac{13C}{12C}$ ratio of the standard
(0.0112372 as per the Pee Dee Belemnite value) and C_i is the DIC concentration C in box i, in mol m^{-3}.

The calculation in Eq. (A1) backs out the fraction $\frac{13C}{12C}$ in the data or model starting value, multiplies that by the standard
reference value and then by the starting model concentration for DIC, C_i, in each box. This is based on an assumption that
the fraction $\frac{13C}{12C}$ is the same as $\frac{13C}{\text{total carbon}}$. For example, there are three isotopes of carbon, each with different atomic weights.
20 They occur in roughly the following abundances: ^{12}C ~98.89%, ^{13}C ~1.11% and ^{14}C ~1x10^{-10}%. Therefore, an assumption
of $\frac{13C}{12C} = \frac{13C}{\text{total carbon}}$, is an approximation, but it is close. Once converted from δ^{13}C (‰) to ^{13}C in mol m^{-3}, the model's ocean
parameters can operate on ^{13}C concentrations in each box, according to the same model flux equations set out in this paper.
The ^{13}C model results are then converted back into δ^{13}C notation at the end of the model run, in order to compare the model
output with data which is reported in δ^{13}C format. The same method is applied to Δ^{14}C. The reference standard value for $\frac{14C}{12C}$
25 is 1.2x10^{-12} as per Craig (1969). Where fractionation of carbon isotopes takes place, fractionation factors are simply added to
the model flux equations as per below.

A1.1 Biological fractionation of carbon isotopes

Biological processes change the carbon isotopic composition of the ocean. When photosynthetic organisms form near the ocean surface, they preferentially partition ^{12}C, the lighter carbon isotope, thereby enriching the surface box in ^{13}C and relatively enriching the underlying boxes in ^{12}C during remineralisation. As such, the ocean displays depletion in δ^{13}C in the deep ocean relative to the shallow ocean (e.g. Curry and Oppo, 2005). A fractionation factor, f, is simply multiplied by the biological flux in Eq. (13) to calculate marine biological fractionation of ^{13}C:

$$\left[\frac{d^{13}C_i}{dt}\right]_{^{13}bio} = f * S_{st} \tag{A2}$$

Where f is the biological fractionation factor for stable carbon (e.g. $\sim$0.977 in Toggweiler and Sarmiento (1985)), and S_{st} is the ratio of ^{13}C to ^{12}C in the reference standard. The typical δ^{13}C composition of marine organisms is in the range -23 to -30‰. The same method is applied for biological fractionation of ^{14}C, but with a different fractionation factor (Toggweiler and Sarmiento, 1985).

A1.2 Fractionation of carbon isotopes during air-sea gas exchange

Fractionation of carbon isotopes also takes place during air-sea exchange. The lighter isotope, ^{12}C, preferentially partitions into the atmosphere. This leads to the heavily depleted δ^{13}C signature for the atmosphere, relative to the ocean. The approach to capture this effect is per Siegenthaler and Munnich (1981):

$$\left[\frac{d^{13}C_i}{dt}\right]_{^{13}gas} = \lambda[\tau R_{At}pCO_{2At} - \pi R_i pCO_{2i}] \tag{A3}$$

Where λ is a kinetic fractionation factor. The λ "kinetic fractionation effect" (Zhang et al., 1995) accounts for the slower equilibration rate of carbon isotopes ^{13}C and ^{14}C across the air-sea interface, compared with ^{12}C (Zhang et al., 1995). R_{At} is the ratio of ^{13}C to ^{12}C in the atmosphere, R_i is the ratio of ^{13}C to ^{12}C in surface ocean box i. pCO_{2At} is the atmospheric pCO_2 and pCO_{2i} is the pCO_2 in the surface ocean boxes. τ and π are the fractionation factors of carbon isotope from air to sea and sea to air respectively. These are temperature dependent and are calculated using the method of Mook et al. (1974), although there are other estimates in the literature (e.g. Zhang et al., 1995). Siegenthaler and Munnich (1981) estimated air-sea $\frac{^{13}C}{^{12}C}$ fractionation in the range -1.8 to -2.3‰, and sea-air fractionation in the range -9.7 to -10.2‰ using a range of estimation methods and temperatures.

A1.3 Source and decay of radiocarbon

Natural radiocarbon is produced in the atmosphere from the collision of cosmic ray produced neutrons with nitrogen. The production rate is variable over time and can be influenced by changes in solar winds and the earth's geomagnetic field intensity (Key, 2001). A mean production rate of 1.57 atom m^{-2} s^{-1} was estimated from the long term record preserved in tree-rings although more recent estimates approach 2 atom m^{-2} s^{-1}(Key, 2001). For use in the model, this estimate needs to be converted

into mols s^{-1}. We first convert atoms to mols by dividing through by Avogrado's number ($\sim$6.022x10^{23}). The resultant figure is multiplied by the earth's surface area ($\sim$5.1x10^{18} cm^{-2}) to yield a production rate of 1.3296x10^{-5} mols s^{-1}. This source rate, divided through by the molar volume of the atmosphere, is added to the solution for atmospheric radiocarbon. A decay timescale for radiocarbon of 8,267 years, is applied to each box in the model.

5 *Author contributions.* CO undertook model build, data-gathering, modelling and model-data experiments. AH provided the oceanographic interpretation, supervised model design, modelling work and designed the model-data experiments. ME provided input into model design, designed model-data experiments and oversaw the modelling of the marine biology and isotopes. BO provided input into model design, oversaw the modelling of carbonate chemistry, marine sediments and interpretation of LGM-Holocene hypotheses. SE designed model-data experiments and oversaw the modelling of the marine biology and carbonate pump. All authors contributed to drafting and reviewing the

10 document.

Competing interests. The authors declare that they have no conflict of interest.

Acknowledgements. Stewart Fallon provided guidance and spreadsheet tools for the processing of radiocarbon data. Malcolm Sambridge provided input on model-data optimisation and inversions. Jimin Yu provided helpful discussions and data.

Appendix B: Parameters, data sources and dimensions

Model item	Value	Source
Ocean surface area (m^2)	3.619×10^{14}	https://www.ngdc.noaa.gov/mgg/global/etopo1_ocean_volumes.html
Average ocean depth (m)	$4,000$	https://www.ngdc.noaa.gov/mgg/global/etopo1_ocean_volumes.html
Mass of the atmosphere (kg)	5.1×10^{18}	https://nssdc.gsfc.nasa.gov/planetary/factsheet/earthfact.html
Mean molecular weight of atmosphere (moles $gram^{-1}$)	28.97	https://nssdc.gsfc.nasa.gov/planetary/factsheet/earthfact.html
Temperature and salinity of the ocean	Various	GLODAPv2 dataset (https://www.nodc.noaa.gov/ocads/oceans/GLODAPv2/)
Modern ocean element concentrations	Various	GLODAPv2 dataset (https://www.nodc.noaa.gov/ocads/oceans/GLODAPv2/)
Ψ_1 global overturning circulation (Sv)	29.0	Talley (2013)
Ψ_2 NADW overturning (Sv)	19.0	Talley (2013)
γ_1 abyssal-deep mixing parameter (Sv)	19.0	Talley (2013)
γ_2 thermocline mixing (Sv)	40	Toggweiler (1999)
Z biological soft carbon productivity @ 100m (mol C m^{-2} yr^{-1})	$1-7$	Martin et al. (1987)
Martin b scalar value	0.75	Berelson (2001)
Air-sea exchange velocity (m day^{-1})	3.0	Toggweiler (1999)
^{13}C air-sea fractionation factors	$0.9989-0.999$	Mook et al. (1974)
^{14}C air-sea fractionation factors	$0.98-0.998$	Toggweiler and Sarmiento (1985)
^{13}C "thermodynamic" air-sea factor	0.99915	Schmittner et al. (2013)
^{14}C "thermodynamic" air-sea factor	0.999	Toggweiler and Sarmiento (1985)
Organic δ^{13}C fractionation factor	~0.975	Toggweiler and Sarmiento (1985)
C/P in org "Redfield ratio"	130	Takahashi et al. (1985)
Rain ratio (carbonate:org in sinking particles)	0.07	Sarmiento et al. (2002)
$CaCO_3$ dissolution rate (units day^{-1})	0.38	Hales and Emerson (1997)
n order of $CaCO_3$ dissolution reaction rate	1.0	Hales and Emerson (1997)
K_{sp} solubility coefficient for calcite	Various	Mucci (1983)
Carbon chemistry solubility and dissociation coefficients	Various	Weiss (1974), Lueker et al. (2000)
Atmosphere radiocarbon production rate (atoms s^{-1})	~1.6	Key (2001)
Suess and bomb radiocarbon corrections	Various	Broecker et al. (1980), Key (2001), Sabine et al. (2004), Eide et al. (2017)
Radiocarbon decay rate (yr^{-1})	1/8267	Stuiver and Polach (1977)
Volcanic emissions flux CO_2 (mol C yr^{-1})	$5\text{-}6 \times 10^{12}$	Modified from Toggweiler (2007)
River phosphorus flux (Tg yr^{-1})	15.0	Compton et al. (2000)

Table 4. SCP-M model dimensions, model parameter starting values and starting data used for model spin-up.

References

Adkins, J., McIntyre, K., and Schrag, D.: The Salinity, Temperature, and 18O of the Glacial Deep Ocean, Science, 298, 2002.

Amiotte Suchet, P., Probst, J., and Ludwig, W.: Worldwide distribution of continental rock lithology: Implications for the atmospheric/soil CO2 uptake by continental weathering and alkalinity river transport to the oceans, Global Biogeochemical Cycles, 17, 7–1 – 7–14, 2003.

Anderson, L. A. and Sarmiento, J. L.: Redfield ratios of remineralization determined by nutrient data analysis, Global Biogeochem. Cycles, 8, 65–80, 1994.

Anderson, R. F., Fleishera, M. Q., Laoc, Y., and Winckler, G.: Modern CaCO3 preservation in equatorial Pacific sediments in the context of late-Pleistocene glacial cycles, Marine Chemistry, 2007.

Annan, J. and Hargreaves, J. C.: A new global reconstruction of temperature changes at the Last Glacial Maximum, Climate of the Past, 9, 367–376, 2013.

Archer, D. and Maier-Reimer, E.: Effect of deep-sea sedimentary calcite preservation on atmospheric CO2 concentration, Nature, pp. 260–263, 1994.

Barker, S., Knorr, G., Vautravers, M., Diz1, P., and Skinner, L.: Extreme deepening of the Atlantic overturning circulation during deglaciation, Nature Geoscience, 3, 2010.

Battaglia, G., Steinacher, M., and Joos, J.: A probabilistic assessment of calcium carbonate export and dissolution in the modern ocean, Biogeosciences, pp. 2823–2848, 2016.

Berelson, W.: The flux of particulate organic carbon into the ocean interior: A comparison of four U.S. JGOFS regional studies, Oceanography, 14, 59–67, 2001.

Boden, T., Marland, G., and Andres, R.: Global, Regional, and National Fossil-Fuel CO2 Emissions, Carbon Dioxide Information Analysis Center, Oak Ridge National Laboratory, U.S. Department of Energy, 2017.

Broecker, W. S.: Ocean chemistry during glacial time, Geochim. Cosmochim. Acta, 46, 1689–1705, 1982.

Broecker, W. S.: The great ocean conveyor, Oceanography, 4, 79–89, 1991.

Broecker, W. S., Peng, T. H., and Engh, R.: Modeling the carbon system, Radiocarbon, 22, 1980.

Bryan, S., Marchitto, T., and Lehman, S.: The release of 14C-depleted carbon from the deep ocean during the last deglaciation: Evidence from the Arabian Sea, Earth and Planetary Science Letters, pp. 244–254, 2010.

Burke, A. and Robinson, L.: The Southern Ocean's Role in Carbon Exchange During the Last Deglaciation, Science, 335, 557–561, 2012.

Chen, T., Robinson, L., Burke, A., Southon, J., Spooner, P., Morris, P., and Ng, H.: Synchronous centennial abrupt events in the ocean and atmosphere during the last deglaciation, Science, 349, 1537–1541, 2015.

Ciais, P., Tagliabue, A., Cuntz, M., Bopp, L., Scholze, M., Hoffmann, G., Lourantou, A., Harrison, S. P., Prentice, I. C., Kelley, D. I., Koven, C., and Piao, S. L.: Large inert carbon pool in the terrestrial biosphere during the Last Glacial Maximum, Nature Geoscience, 5, 74–79, 2012.

Compton, J., Mallinson, D., Glenn, C., and Zanin, Y.: Variations in the global phosphorus cycle, vol. 66, pp. 21–33, Society of Sedimentary Geology, 2000.

Craig, H.: The natural distribution of radiocarbon and the exchange time of carbon dioxide between atmosphere and sea, Tellus, 9, 1–17, 1957.

Craig, H.: Abyssal carbon and radiocarbon in the Pacific, J. Geophys. Res., 74, 5491–5506, 1969.

Curry, W., Duplessy, J., Labeyrie, L., and Shackleton, N.: Changes in the distribution of d13C of deep water PCO2 between the last glaciation and the Holocene, Paleoceanography, 3, 1988.

Curry, W. B. and Oppo, D. W.: Glacial water mass geometry and the distribution of d13C of CO2 in the western Atlantic Ocean, Paleoceanography, 20, 2005.

5 Davies-Walczak, M., Mix, A., Stoner, J., Southon, J., Cheseby, M., and Xuan, C.: Late Glacial to Holocene radiocarbon constraints on North Pacific Intermediate Water ventilation and deglacial atmospheric CO2 sources, Earth and Planetary Science Letters, pp. 57–66, 2014.

De Boer, A. M. and Hogg, A. M. C.: Control of the glacial carbon budget by topographically induced mixing, Geophys. Res. Lett, 41, 4277–4284, 2014.

de Boyer Montegut, C., Madec, G., Fischer, A. S., Lazar, A., and Iudicone, D.: Mixed layer depth over the global ocean: An examination of 10 profile data and a profile based climatology, Journal of Geophysical Research, 109, 2004.

Dickson, R. R. and Brown, J.: The production of North Atlantic Deep Water: Sources, rates, and pathways, Journal of Geophysical Research, pp. 319–341, 1994.

Eide, M., Olsen, A., Ninnemann, U. S., and Eldevik, T.: A global estimate of the full oceanic 13C Suess effect since the preindustrial, Global Biogeochemical Cycles, 2017.

15 Emerson, S. and Hedges, J. I.: Sediment diagenesis and benthic flux. In: Treatise on Geochemistry, vol. 6, Elsevier, Amsterdam, 2003.

Fallon, S.: Pers comm, 2018.

Farrell, J. and Prell, W. L.: Climatic change and CaCO3 preservation: An 800,000 year bathymetric reconstruction from the central equatorial Pacific Ocean, Paleoceanography, 4, 447–466, 1989.

Ferrari, R., Jansen, M., Adkins, J., Burke, A., Stewart, A. L., and Thompson, A.: Antarctic sea ice control on ocean circulation in present and 20 glacial climates, PNAS, 111, 8753–8758, 2014.

Follows, M. J., Ito, T., and Dutkiewicz, S.: On the solution of the carbonate chemistry system in ocean biogeochemistry models, Ocean Modelling, 12, 290–30, 2006.

Francois, L., Godderis, Y., Warnant, P., Ramstein, G., de Noblet, N., and Lorenz, S.: Carbon stocks and isotopic budgets of the terrestrial biosphere at mid-Holocene and last glacial maximum times, Chemical Geology, 159, 163–199, 1999.

25 Gebbie, G., Peterson, C., Lisiecki, L., and Spero, H.: Global-mean marine d13C and its uncertainty in a glacial state estimate, Quaternary Science Reviews, pp. 144–159, 2015.

Gordon, A.: The role of thermohaline circulation in global climate change, Lamont-Doherty Geological Observatory Report 1990/91, pp. 44–51, 1991.

Grant, K. M., Rohling, E. J., Ramsey, C. B., Cheng, H., Edwards, R. L., Florindo, F., Heslop, D., Marra, F., Roberts, A. P., Tamisiea, M. E., 30 and Williams, F.: Sea-level variability over five glacial cycles, Nature Communications, 5, 2014.

Hain, M. P., Sigman, D. M., and Haug, G. H.: Carbon dioxide effects of Antarctic stratification, North Atlantic Intermediate Water formation, and subantarctic nutrient drawdown during the last ice age: Diagnosis and synthesis in a geochemical box model, Global Biogeochem. Cycles, 24, 2010.

Hales, B. and Emerson, S.: Evidence in support of first-order dissolution kinetics of calcite in seawater, Earth and Planetary Science Letters, 35 148, 317–327, 1997.

Harman, I., Trudinger, C., and Raupach, M.: SCCM – the Simple Carbon-Climate Model: Technical Documentation, CAWCR Technical Report 047, CSIRO Centre for Australian Weather and Climate Research, CSIRO Marine and Atmospheric Research, FC Pye Laboratory, GPO Box 3023, Canberra, ACT, 2601, Australia, 2011.

Harrison, W., Head, E., Horne, E., B.Irwin, Li, W., Longhurst, A., Paranjape, M., and Platt, T.: The western North Atlantic bloom experiment, Deep Sea Research Part II: Topical Studies in Oceanography, 40, 1993.

Henson, S. A., Sanders, R., Madsen, E., Morris, P. J., Moigne, F. L., and Quartly, G. D.: A reduced estimate of the strength of the ocean's biological carbon pump, Geophys. Res. Lett., 38, 2011.

5   Hesse, T., Butzin, M., Bickert, T., and Lohmann, G.: A model data comparison of d13C in the glacial Atlantic Ocean, Paleoceanography, 26, 2011.

Hines, S., Southon, J., and Adkins, J.: A high-resolution record of Southern Ocean intermediate water radiocarbon over the past 30,000 years, Earth and Planetary Science Letters, pp. 46–48, 2015.

Hogg, A. M. C.: Glacial cycles and carbon dioxide: A conceptual model, Geophys. Res. Lett., 35, 2008.

10   Houghton, R.: How well do we know the flux of CO2 from land-use change?, Tellus B: Chemical and Physical Meteorology, 62, 337–351, 2010.

IPCC: Annex II: Climate System Scenario Tables. In: Climate Change 2013: The Physical Science Basis. Contribution of Working Group I to the Fifth Assessment Report of the Intergovernmental Panel on Climate Change, pp. 1395–1445, Cambridge University Press, Cambridge, United Kingdom and New York, NY, USA, 2013.

15   Jansen, H., Zeebe, R., and Wolf-Gladrow, D.: Modeling the dissolution of settling CaCO3 in the ocean, Global Biogeochemical Cycles, 16, 11–1 – 11–15, 2002.

Jones, C., Robertson, E., Arorab, V., Friedlingstein, P., Shevliakova, E., Bopp, L., Brovkin, V., Hajima, T., Kato, E., Kawamiya, M., S., Liddicoat, Lindsay, K., Reick, C., Roelandt, C., Segschneider, J., and Tjiputra, J.: Twenty-First-Century Compatible CO2 Emissions and Airborne Fraction Simulated by CMIP5 Earth System Models under Four Representative Concentration Pathways, Journal of Climate, 26,
20   2013.

Keeling, C. and Bolin, B.: The simultaneous use of chemical tracers in oceanic studies 11. A three-reservoir model of the North and South Pacific Oceans, Tellus, 20, 17–53, 1968.

Key, R.: Ocean process tracers: Radiocarbon. In: Encyclopedia of Ocean Sciences, pp. 2338–2353, Academic Press, London, 2001.

Klaas, C. and Archer, D. E.: Association of sinking organic matter with various types of mineral ballast in the deep sea: Implications for the
25   rain ratio, Global Biogeochem. Cycles, 16, 2002.

Knox, F. and McElroy, M.: Changes in Atmospheric CO2: Influence of the Marine Biota at High Latitude, Journal of Geophysical Research, 89, 4269–4637, 1984.

Kuhlbrodt, T. A., Griesel, M., Montoya, A., Levermann, M., Hofmann, M., and Rahmstorf, S.: On the driving processes of the Atlantic meridional overturning circulation, Reviews of Geophysics, 45, 2007.

30   Liu, C., Kohl, A., Liu, Z., Wang, F., and Stammer, D.: Deep-reaching thermocline mixing in the equatorial pacific cold tongue, Nature Communications, 7:11576, 2016.

Lueker, T. J., Dickson, A. G., and Keeling, C. D.: Ocean pCO2 calculated from dissolved inorganic carbon, alkalinity, and equations for K-1 and K-2: validation based on laboratory measurements of CO2 in gas and seawater at equilibrium, Marine Chemistry, 70, 105–119, 2000.

Lumpkin, R. and Speer, K.: Global ocean meridional overturning, Journal of Physical Oceanography, 37, 550–562, 2007.

35   Lund, D. C., Adkins, J. F., and Ferrari, R.: Abyssal Atlantic circulation during the Last Glacial Maximum: Constraining the ratio between transport and vertical mixing, Paleoceanography, 26, 2011.

Maiti, K., Charette, M. A., Buesseler, K. O., and Kahru, M.: An inverse relationship between production and export efficiency in the Southern Ocean, Geophys. Res. Lett., 40, 1557–1561, 2013.

Marchitto, T., Lehman, S., Ortiz, J., Flückiger, J., and van Geen, A.: Marine Radiocarbon Evidence for the Mechanism of Deglacial Atmospheric CO2 Rise, Science, 316, 2007.

Marcott, S., Bauska, T., Buizert, C., Steig, E., Rosen, J., Cuffey, K., Fudge, T. J., Severinghaus, J. P., Ahn, J., Kalk, M. L., McConnell, J. R., Sowers, T., Taylor, K., White, J. W. C., and Brook, E.: Centennial-scale changes in the global carbon cycle during the last deglaciation, Nature, 514, 2014.

Mariotti, V., Paillard, D., Roche, D., Bouttes, N., and Bopp, L.: Simulated last glacial maximum D14Catm and the deep glacial ocean carbon reservoir, Radiocarbon, 55, 1595–1602, 2013.

Marshall, J. and Speer, K.: Closure of the meridional overturning circulation through Southern Ocean upwelling, Nature Geoscience, 5, 171–180, 2012.

Martin, J. H., Knauer, G., Karl, D., and Broenkow, W.: VERTEX: carbon cycling in the northeast Pacific, Deep-Sea Research, 34, 267–285, 1987.

Mekik, F. A., Anderson, R. F., Loubere, P., François, R., and Richaud, M.: The mystery of the missing deglacial carbonate preservation maximum, Quaternary Science Reviews, 39, 60–72, 2012.

Menviel, L., Yu, J., Joos, F., Mouchet, A., Meissner, K. J., and England, M. H.: Poorly ventilated deep ocean at the Last Glacial Maximum inferred from carbon isotopes: A data-model comparison study, Paleoceanography, 31, 2016.

Millero, F. J.: Influence of pressure on chemical processes in the sea. In Chemical Oceanography, 2nd edn, vol. 8, Academic Press, New York, 1983.

Milliman, J. D., Troy, P. J., Balch, W. M., Adams, A. K., Li, Y.-H., and Mackenzie, F. T.: Biologically mediated dissolution of calcium carbonate above the chemical lysocline?, Deep Sea Research Part I: Oceanographic Research Papers, Part I, 1653–1669, 1999.

Mook, W., Bommerson, J., and Staverman, W.: Carbon Isotope Fractionation Between Dissolved Bicarbonate and Gaseous Carbon Dioxide, Earth and Planetary Science Letters, 22, 169–176, 1974.

Morrison, A. and Hogg, A.: On the Relationship between Southern Ocean Overturning and ACC Transport, Journal of Physical Oceanography, 43, 2013.

Morse, J. W. and Berner, R. A.: Dissolution kinetics of calcium carbonate in sea water. II: A kinetic origin for the lysocline, Am J Sci, 272, 1972.

Mucci, A.: The solubility of calcite and aragonite in seawater at various salinities, temperatures, and one atmosphere total pressure, Am J Sci, 283, 780–799, 1983.

Olsen, A., Key, R. M., van Heuven, S., Lauvset, S. K., Velo, A., Lin, X., Schirnick, C., Kozyr, A., Tanhua, T., Hoppema, M., Jutterström, S., Steinfeldt, R., Jeansson, E., Ishii, M., Pérez, F. F., and Suzuki, T.: The Global Ocean Data Analysis Project version 2 (GLODAPv2) – an internally consistent data product for the world ocean, Earth System Science Data, 8, 297–323, 2016.

Peterson, C. D., Lisiecki, L. E., and Stern, J. V.: Deglacial whole-ocean d13C change estimated from 480 benthic foraminiferal records, Paleoceanography, pp. 549–563, 2014.

Raupach, M., Canadell, J., Ciais, P., Friedlingstein, P., Rayner, P., and Trudinger, C.: The relationship between peak warming and cumulative CO2 emissions, and its use to quantify vulnerabilities in the carbon-climate-human system, Tellus, pp. 145–164, 2011.

Redfield, A. C., Ketchum, B. H., and Richards, F. A.: The influence of organisms on the composition of seawater, The Sea, 2, 26–77, 1963.

Reimer, P., Baillie, M., Bard, E., Bayliss, A., Beck, J., Blackwell, P., Ramsey, C. B., Buck, C., Burr, G., Edwards, R., Friedrich, M., Grootes, P., Guilderson, T., I, I. H., Heaton, T., Hogg, A., Hughen, K., Kaiser, K., Kromer, B., S.W., F. M., Manning, Reimer, R., Richards, D.,

Southon, J., Talamo, S., Turney, C., van der Plicht, J., and Weyhenmeyer, C.: IntCal09 and Marine09 radiocarbon age calibration curves, 0–50,000 years cal BP., Radiocarbon, 51, 1111–50, 2009.

Ronge, T., Tiedemann, R., Lamy, F., Kohler, P., Alloway, B., Pol-Holz, R. D., Pahnke, K., Southon, J., and Wacker, L.: Radiocarbon constraints on the extent and evolution of the South Pacific glacial carbon pool, Nature Communications, 2016.

5 Sabine, C., Feely, R., Gruber, N., Key, R., Lee, K., Bullister, J., Wanninkhof, R., Wong, C., Wallace, D., Tilbrook, B., et al.: The oceanic sink for anthropogenic CO2, Science, pp. 367–371, 2004.

Sarmiento, J. L. and Gruber, N.: Ocean biogeochemical dynamics, Princeton University Press, 2006.

Sarmiento, J. L. and Toggweiler, J. R.: A new model for the role of the oceans in determining atmospheric CO2, Nature, 308, 621–624, 1984.

Sarmiento, J. L., Dunne, J., Gnanadesikan, A., Key, R. M., Matsumoto, K., and Slater, R.: A new estimate of the CaCO3 to organic carbon
10   export ratio, Global Biogeochemical Cycles, 16, 2002.

Schmitt, J., Schneider, R., Elsig, J., Leuenberger, D., Lourantou, A., Chappellaz, J., Köhler, P., Joos, F., Stocker, T., Leuenberger, M., and Fischer, H.: Carbon Isotope Constraints on the Deglacial CO2 Rise from Ice Cores, Science, 336, 2012.

Schmittner, A., Gruber, N., Mix, A. C., Key, R. M., Tagliabue, A., and Westberry, T. K.: Biology and air–sea gas exchange controls on the distribution of carbon isotope ratios in the ocean, Biogeosciences, 10, 5793–5816, 2013.

15 Schmitz, W. J.: On the World Ocean Circulation: Volume I. Some global features/ North Atlantic circulation, Woods Hole Oceanographic Institution Technical Report, WHOI-96-03, 144, 1996.

Siegenthaler, U. and Munnich, K. O.: 13C/12C fractionation during CO2 transfer from air to sea. In: Carbon Cycle Modelling, SCOPE 16, John Wiley, New York, 1981.

Siegenthaler, U. and Wenk, T.: Rapid atmospheric CO2 variations and ocean circulation, Nature, 308, 1984.

20 Sigman, D. and Boyle, E.: Glacial/interglacial variations in atmospheric carbon dioxide, Nature Reviews, 407, 2000.

Sigman, D., Hain, M., and Haug, G.: The polar ocean and glacial cycles in atmospheric CO2 concentration, Nature Reviews, 466, 47–55, 2010.

Sikes, E., Cook, M., and Guilderson, T.: Reduced deep ocean ventilation in the Southern Pacific Ocean during the last glaciation persisted into the deglaciation, Earth and Planetary Science Letters, pp. 130–138, 2016.

25 Skinner, L. and Shackleton, N. J.: Rapid transient changes in northeast Atlantic deep water ventilation age across Termination I, Paleoceanography, 19, 2004.

Skinner, L., McCave, I., Carter, L., Fallon, S., Scrivner, A., and Primeau, F.: Reduced ventilation and enhanced magnitude of the deep Pacific carbon pool during the last glacial period, Earth and Planetary Science Letters, pp. 45–52, 2015.

Skinner, L., Primeau, F., Freeman, E., de la Fuente, M., Goodwin, P. A., Gottschalk, J., Huang, E., McCave, I. N., Noble, T. L., and Scrivner,
30   A. E.: Radiocarbon constraints on the glacial ocean circulation and its impact on atmospheric CO2, Nature Communications, 8, 2017.

Skinner, L. C., Fallon, S., Waelbroeck, C., Michel, E., and Barker, S.: Ventilation of the Deep Southern Ocean and Deglacial CO2 Rise, Science, 328, 1147–1151, 2010.

Stephens, B. and Keeling, R.: The infuence of Antarctic sea ice on glacial-interglacial CO2 variations, Nature, 404, 2000.

Stuiver, M. and Polach, H.: Reporting of 14C data, Radiocarbon, 19, 355–363, 1977.

35 Stuiver, M., Reimer, P., and Braziunas, T.: High-precision radiocarbon age calibration for terrestrial and marine samples, Radiocarbon, 40, 1128–1151, 1998.

Sverdrup, H., Johnson, N., and Fleming, R.: The Oceans., Prentice-Hall,, Englewood Cliffs, NJ, 1941.

Takahashi, T., Broecker, W. S., and Langer, S.: Redfield ratio based on chemical data from isopycnal surfaces, J. Geophys. Res., 90, 6907–6924, 1985.

Talley, L.: Freshwater transport estimates and the global overturning circulation: Shallow, deep and throughflow components, Progress in Oceanography, 78, 257–303, 2008.

5 Talley, L.: Closure of the global overturning circulation through the Indian, Pacific, and Southern Oceans: Schematics and transports, Oceanography, 78, 257–303, 2013.

Toggweiler, J. and Sarmiento, J.: Glacial to interglacial changes in atmospheric carbon dioxide: The critical role of ocean surface water in high latitudes, in The Carbon Cycle and Atmospheric CO2: Natural Variations Archean to Present, Geophysical Monograph Series, American Geophysical Union, 32, 163–184, 1985.

10 Toggweiler, J. R.: Variation of atmospheric CO2 by ventilation of the ocean's deepest water, Paleoceanography, 14, 571–588, 1999.

Toggweiler, J. R.: Origin of the 100,000-yr time scale in Antarctic temperatures and atmospheric CO2, Paleoceanography, 2007.

Trent-Staid, M. and Prell, W. L.: Sea surface temperature at the Last Glacial Maximum:A reconstruction using the modern analog technique, Paleoceanography, 17, 2002.

Turnbull, J., Mikaloff-Fletcher, S., Ansell, I., and Steinkamp, K.: Sixty years of radiocarbon dioxide measurements at Wellington, New 15 Zealand 1954–2014, Atmopheric Chemistry and Physics Discussions, 2016.

Volk, T. and Hoffert, M. I.: Ocean carbon pumps: Analysis of relative strengths and efficiencies in ocean-driven atmospheric CO2 changes, in The Carbon Cycle and Atmospheric CO2: Natural Variations Archean to Present, Geophys. Monogr. Ser, 32, 99–110, 1985.

Wang, L., Huang, J., Luo, Y., and Zhao, Z.: Narrowing the spread in CMIP5 model projections of air-sea CO2 fluxes, Nature Scientific Reports, 6, 2016.

20 Watson, A., Vallis, G. K., and Nikurashin, M.: Southern Ocean Buoyancy Forcing of Ocean Ventilation and Glacial Atmospheric CO2, Nature Geosciences (in review), 2015.

Weiss, R.: Carbon dioxide in water and seawater: the solubility of a non ideal gas, Marine Chemistry, 8, 1974.

Yokoyama, Y., Lambeck, K., Deckker, P. D., Johnston, P., and Field, K.: Timing of the Last Glacial Maximum from observed sea-level minima, Nature, 406, 713–716, 2000.

25 Yu, J., Anderson, R., Z.Jin, Menviel, L., Zhang, F., Ryerson, F., and Rohling, E.: Deep South Atlantic carbonate chemistry and increased interocean deep water exchange during last deglaciation, Quaternary Science Reviews, pp. 80–89, 2014a.

Yu, J., Anderson, R. F., and Rohling, E. J.: Deep ocean carbonate chemistry and glacial-interglacial atmospheric CO2 changes, Oceanography, 27, 2014b.

Zeebe, R.: OSCAR: Long-term Ocean-atmosphere-Sediment Carbon cycle Reservoir Model v2.0.4, Geosci. Model Dev., 5, 149–166, 2012.

30 Zeebe, R. E. and Wolf-Gladrow, D. A.: CO2 in seawater: equilibrium, kinetics, isotopes, Elsevier Oceanography Series, Elsevier, Amsterdam, 2001.

Zhang, J., Quay, P., and Wilbur, D.: Carbon isotope fractionation during gas-water exchange and dissolution of CO2, Geochimica et Cosmochimica Acta, 59, 107–114, 1995.

Zhao, N., Marchal, O., Keigwin, L., Amrhein, D., and Gebbie, G.: A Synthesis of Deglacial Deep-Sea Radiocarbon Records and Their 35 (In)Consistency With Modern Ocean Ventilation, Paleoceanography and Paleoclimatology, 33, 128–151, 2017.